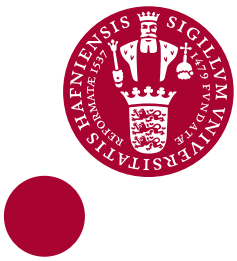

A New Process-Based Soil Methane Scheme

Evaluation Over Arctic Field Sites With the ISBA Land Surface Model

Morel, X.; Decharme, B.; Delire, C.; Krinner, G.; Lund, M.; Hansen, B. U.; Mastepanov, M.

Published in:
Journal of Advances in Modeling Earth Systems

DOI:
10.1029/2018MS001329

Publication date:
2019

Document version
Publisher's PDF, also known as Version of record

JAMES | Journal of Advances in Modeling Earth Systems

RESEARCH ARTICLE
10.1029/2018MS001329

A New Process-Based Soil Methane Scheme: Evaluation Over Arctic Field Sites With the ISBA Land Surface Model

X. Morel[1], B. Decharme[1], C. Delire[1], G. Krinner[2], M. Lund[3], B. U. Hansen[4], and M. Mastepanov[3,5]

[1]CNRM UMR 3589, Meteo-France/CNRS, Toulouse, France, [2]Laboratoire de Glaciologie et Geophysique de l'Environnement, Grenoble, France, [3]Department of Bioscience, Arctic Research Centre, Aarhus University, Roskilde, Denmark, [4]Center for Permafrost, Department of Geosciences and Natural Resource Management, University of Copenhagen, Copenhagen, Denmark, [5]Department of Physical Geography and Ecosystem Science, Lund University, Lund, Sweden

Key Points:
- A vertically discretized soil carbon and methane emission module controlled by the O_2 profile is developed
- New parametrization of gas bulk diffusivity, methanotrophy, and ebullition are introduced; representations of many processes are revisited
- The model correctly represents methane fluxes and subsurface processes at three arctic sites, with and without permafrost

Correspondence to:
X. Morel,
morelxavier1@gmail.com

Citation:
Morel, X., Decharme, B., Delire, C., Krinner, G., Lund, M., Hansen, B. U. & Mastepanov, M. (2019). A new process-based soil methane scheme for land surface modeling: Evaluation over arctic field sites with the ISBA land surface model. *Journal of Advances in Modeling Earth Systems*, *11*, 293–326. https://doi.org/10.1029/2018MS001329

Received 22 MAR 2018
Accepted 17 DEC 2018
Accepted article online 18 DEC 2018
Published online 27 JAN 2019

Abstract Permafrost soils and arctic wetlands methane emissions represent an important challenge for modeling the future climate. Here we present a process-based model designed to correctly represent the main thermal, hydrological, and biogeochemical processes related to these emissions for general land surface modeling. We propose a new multilayer soil carbon and gas module within the Interaction Soil-Biosphere-Atmosphere (ISBA) land-surface model (LSM). This module represents carbon pools, vertical carbon dynamics, and both oxic and anoxic organic matter decomposition. It also represents the soil gas processes for CH_4, CO_2, and O_2 through the soil column. We base CH_4 production and oxydation on an O_2 control instead of the classical water table level strata approach used in state-of-the-art soil CH_4 models. We propose a new parametrization of CH_4 oxydation using recent field experiments and use an explicit O_2 limitation for soil carbon decomposition. Soil gas transport is computed explicitly, using a revisited formulation of plant-mediated transport, a new representation of gas bulk diffusivity in porous media closer to experimental observations, and an innovative advection term for ebullition. We evaluate this advanced model on three climatically distinct sites : two in Greenland (Nuuk and Zackenberg) and one in Siberia (Chokurdakh). The model realistically reproduces methane and carbon dioxide emissions from both permafrosted and nonpermafrosted sites. The evolution and vertical characteristics of the underground processes leading to these fluxes are consistent with current knowledge. Results also show that physics is the main driver of methane fluxes, and the main source of variability appears to be the water table depth.

1. Introduction

Methane (CH_4) is the second most important anthropogenic greenhouse gas. Since preindustrial times, the concentration of CH_4 has increased by approximately 150%, from 772 $\pm$ 25 ppb in 1750 to 1803 $\pm$ 2 ppb in 2006 (Intergovernmental Panel on Climate Change, 2013). After a small hiatus at the beginning of the century, atmospheric methane concentration has continuously increased. Although its atmospheric concentration is much smaller than that of carbon dioxide (CO_2), the methane global warming potential is 28 to 32 times higher when integrated over a 100-year period (Etminan et al., 2016; Myhre et al., 2013), and it contributes to about 20% of the radiative forcing from greenhouse gases. Atmospheric CH_4 concentration results from the balance between methane sources and sinks. Methane is emitted by a variety of sources, both anthropogenic and natural, and is mainly of biological origin. Biogenic methane comes from the decomposition of organic matter by methanogenic archaea in anaerobic environments, such as wetlands (e.g., swamps, peatlands, fen, or rice paddies; Saunois et al., 2016) and high-latitude lakes (Wik et al., 2016). When integrated at the global scale, wetlands are the largest source of methane for the atmosphere and also the most uncertain (Ciais et al., 2013; Kirschke et al., 2013). On a global scale, simulated CH_4 emissions from the WETCHIMP model intercomparison project range from 141 Tg CH_4/year to 264 Tg CH_4/year (Melton et al., 2013). It has been estimated that northern latitude wetlands account for one third to half of the methane emissions from natural wetlands (Schlesinger & Bernhardt, 2013). These high-latitude wetlands are of particular interest because they are located where the impact of future climate is expected to be

the most pronounced, and it is still unclear how the emissions from northern wetlands will respond to these changes (Riley et al., 2011).

One natural source of methane is permafrost, which is defined as frozen soil, sediment, or rock with temperatures at or below 0 °C for at least two consecutive years. These freezing temperatures prevent organic matter in permafrost from decaying and decomposing (Schirrmeister et al., 2011; Smith, 2004; Zimov, 2006). According to recent estimates at global scale, soils contain about 2000 Pg of carbon (C) in the top 2 m (Shangguan et al., 2014). A large fraction of this terrestrial carbon stock is located in permafrost soils, mostly located in the upper part of permafrost soils: around 1035 PgC in the top 3 m and another 272 PgC below (Hugelius et al., 2014). The latter fraction is mainly buried within the Yedoma ice complex. Overall, these estimations have some significant uncertainties, mainly due to large data gaps and to the inherent vastness and remoteness of these regions (Ping et al., 2015). Soil thaw dynamics are an important factor both for seasonal and interannual subsurface processes. Most gases emitted from the soil originate from the active layer, that is, the upper soil layer, which thaws in summer. Inert carbon stocks play a critical role in the terrestrial feedbacks to climate change; as permafrost thaws, the previously frozen carbon starts to decompose, releasing greenhouse gases into the atmosphere. These emissions from terrestrial ecosystems have the potential to increase climate warming in a positive feedback loop (Burke et al., 2012, 2013; Koven et al., 2011; MacDougall et al., 2012; Schaefer et al., 2014; Schneider Von Deimling et al., 2015; Schuur et al., 2015). Current studies suggest that there will be 35–205 Pg of permafrost carbon emissions by the year 2100 (Schaefer et al., 2014; Schuur et al., 2015). The magnitude and timing of these carbon fluxes remain highly uncertain (Song et al., 2012), partly because of incomplete observations and partly because modeling of many of the relevant processes is still relatively new (Saunois et al., 2016).

Net methane flux is the result of two sequential and antagonistic processes: methanogenesis, the production of methane, which takes place in the anoxic part of the soil, and methanotrophy, the methane oxidation, which takes place in the oxic part of the soil. There are three pathways for soil methane to reach the atmosphere: diffusion, ebullition, and plant-mediated transport (PMT). Both environmental and biotic factors influence the production, oxidation, and transport of methane in the soil. These processes have been modeled in various ways, with complexities ranging from empirical to process based (Cao et al., 1996; Kaiser et al., 2016; Khvorostyanov et al., 2008; Petrescu et al., 2010; Raivonen et al., 2017; Tang et al., 2013; Walter & Heimann, 2000; Wania et al., 2010; Zhang et al., 2012; Zhu et al., 2014; Zhuang et al., 2004). The detailed review by Xu et al. (2016) shows that the models differ in the mathematical formulation of the represented processes and in the parameter values even when the same formulation is chosen. These differences are partly due to the wide range in the observed magnitude of biogeochemical processes such as methanotrophy and methanogenesis (Segers, 1998). Due to these intrinsic uncertainties of parameters, methane model results are broad and diverse on the global scale (Melton et al., 2013) : indeed, they are quite sensitive to the set of parameters of many processes described in the literature (Meng et al., 2012). The same holds true for regional scale modeling (Bohn et al., 2015) and at the site level, where the degree of complexity chosen to describe individual processes can substantially change model behavior (Tang et al., 2010).

The aim of this paper is to describe and evaluate a new soil biogeochemical carbon and greenhouse gas emissions model embedded in the land surface model Interaction Soil-Biosphere-Atmosphere (ISBA; Noilhan & Planton, 1989). The model has a vertically discretized representation of soil carbon and explicitly represents CO_2, CH_4, and O_2 within the soil, along with their interactions with biogeochemical processes, their transport through the soil column, and their exchange between the soil and the atmosphere. Vertical dynamics processes affect the carbon pools. Unlike many existing multilayer models whose common feature is the use of the water table to directly discriminate regions of methane production and methane oxidation (e.g., Kaiser et al., 2016; Riley et al., 2011; Tang et al., 2013; Walter & Heimann, 2000; Wania et al., 2010), we propose a new formulation based on O_2 concentration within the soil, inspired by Khvorostyanov et al. (2008). Methanotrophy temperature dependency is taken from recent field and incubation experiments (Jørgensen et al., 2015). Transport of gases through the soil is described mechanistically, with a new nonlinear formulation for diffusion closer to experimental results, a PMT formulation inspired by Riley et al. (2011) and a new layer-by-layer ebullition algorithm. Embedded in a land surface model, hydrological, thermal, biogeochemical, and carbon cycle processes are coupled and solved using the same vertical discretization. Environmental controls are hence calculated by the model. Finally, substrate for methanogenesis and oxic decomposition is the modeled soil carbon pools. Overall, the model ranges between the second and third clusters defined in Xu et al. (2016) analysis.

In section 2, we describe the original bulk carbon module embedded in ISBA then its discretization. We further detail in section 2.2 the greenhouse gas emission module, stressing how it differs from existing models, in particular for the methanotrophy. The three sites and the experimental protocol are detailed in section 3. In section 4, we evaluate the model on three sites: two in Greenland and one in Siberia. We first evaluate whether physical variables such as energy balance, snow depth, and soil temperatures are well reproduced by ISBA and subsequently evaluate methane and carbon dioxide modeled emissions against observations. We discuss in section 5 the model's in-depth behavior, in terms of soil gas profiles and soil processes. We then present sensitivity analyses focusing primarily on the water table level, temperature dependency of methanogenesis, and methanotrophy impact on resulting methane fluxes. Finally, we discuss some biotic factors not taken into account in the model.

2. Model Description

The ISBA land surface model (Noilhan & Planton, 1989) represents the energy, water, and carbon budget of the land surface. ISBA is embedded in the SURFEX (SUR-Face EXternalized) modeling platform (Masson et al., 2013) and used in all atmospheric mesoscale, regional scale, and global scale models of Meteo-France, as well as in regional hydrological forecasting systems and global hydrological models. It was evaluated over many local or regional field data sets (Decharme et al., 2011, 2013, 2016; Garrigues et al., 2018; Joetzjer et al., 2015; Séférian et al., 2016). The ISBA scheme solves the energy and hydrological budget using a multilayer approach for the soil (Boone et al., 2000; Decharme et al., 2011) and for the snowpack (Boone & Etchevers, 2001; Decharme et al., 2016). The hydraulic and thermal properties of soil depend on the soil texture and organic matter (Decharme et al., 2016). The physical model is discretized into 14 soil layers, with a finer resolution on the upper soil and a coarser one at the bottom. The standard total depth is 12 m but can be changed if needed. The energy budget is always solved up to this depth, regardless of soil type and plant functional type. The model uses a power distribution for vertical root distribution based on Jackson et al. (1996). The water budget is solved down to the rooting depth, which depends on the plant functional type (Decharme et al., 2013). However, for permafrost soils, the water budget is solved down to 12 m, regardless of vegetation, to correctly represent freezing and thawing (Decharme et al., 2016).

Vegetation in ISBA is represented by 16 plant functional types, including a boreal *C*3 grass type used in this work, and three land cover types. The model represents carbon cycling in vegetation and soils. Leaf level photosynthesis and respiration are calculated using the approach of Goudriaan (1986), implemented by Calvet et al. (1998). Leaf phenology results directly from the simulated carbon balance of the canopy. The model represents six biomass pools for trees and three for grasses (Gibelin, 2007; Joetzjer et al., 2015). Mortality is represented simply by a turnover term. Dead plant material forms litter reservoirs that are decomposed to form the soil carbon pools.

2.1. Soil Organic Carbon Module

2.1.1. The Original Bulk Carbon Module

The original ISBA litter and soil carbon module is based on the CENTURY bulk carbon model (Parton et al., 1988). It describes organic litter and soil carbon pools, corresponding to different states of decomposition characterized by different residence times τ_i (s), and the fluxes between them. It simulates four litter pools: two pools of aboveground litter $C_{ab,[s,m]}$ composed of dead leaves and branches and two pools of belowground litter $C_{bg,[s,m]}$ formed by dead roots. The aboveground and belowground litter pools are further separated into a structural carbon pool $C_{[ab,bg],s}$, made of cellulose and lignin from dead biomass, and a metabolic carbon pool $C_{[ab,bg],m}$, made of easily degradable organic compounds. The model simulates three pools of soil organic matter (SOM), receiving organic matter from the decomposition of litter pools. The active carbon pool C_a represents the freshest and most labile organic carbon. The slow carbon pool C_s represents organic carbon with a stronger resistance to decomposition, due to either a physical barrier or its chemical form. The passive carbon pool C_p represents physically protected or chemically recalcitrant carbon. These different pools do not represent distinct physical entities but rather different chemical states of organic matter. Values of residence time τ_i for heterotrophic respiration are taken from the STOMATE carbon model, used in the IPSL Earth System Model ORCHIDEE (Gibelin et al., 2006; Krinner et al., 2005). Table 1 represents characteristic residence times for these pools.

Table 1
Residence Times for the Seven Model Carbon Pools

Carbon pool	Residence time τ (year)
Above-ground structural litter $C_{[ab,s]}$	0.245
Above-ground metabolic litter $C_{[ab,m]}$	0.066
Below-ground structural litter $C_{[bg,s]}$	0.245
Below-ground metabolic litter $C_{[bg,m]}$	0.066
Active carbon pool C_a	0.149
Slow carbon pool C_s	5.48
Passive carbon pool C_p	241

Following this parametrization, the SOM is decomposed and passed through a cascade of different pools, releasing CO_2 as respiration in each step. Equation (1) represents the time evolution of a carbon pool C_i

$$\frac{\partial C_i}{\partial t} = S_i + \sum_{j \neq i} (1 - r_j) f_{ji} F^j_{\text{oxic}} - F^i_{\text{oxic}} \tag{1}$$

where t is the time, S_i the input from the vegetation and roots exudates into the corresponding litter reservoirs $i = [(ab, bg), (s, m)]$ (for the three SOM pools, S_i is zero), r_j is the fraction of the decomposed material of the carbon pool C_j lost as respiration, and f_{ji} the fraction of carbon pool j transformed into pool i. r_i and f_{ij} depend on the sand fraction and, for the litter pools, on the lignin ratio. Values and parametrization of these fractions are issued directly from CENTURY (Parton et al., 1988). F^i_{oxic} is the quantity of carbon decomposed in the pool i. Its dependence on temperature and soil moisture is defined as follows:

$$F^i_{\text{oxic}} = k_i \theta C_i \tag{2}$$

where k_i (s^{-1}), the effective decomposition rate depending on soil temperature T_g (°C), is given by

$$k_i(T_g) = \frac{1}{\tau_i} Q_{10}^{\frac{T_g - T_{\max}}{10}} \tag{3}$$

The organic matter decomposition rate k_i increases with temperature. We use the classical exponential Q_{10} function, with a Q_{10} value of 2 and a $T_{\max}$ of 30 °C (Figure 2a). However, there is no consensus on the type of relationship that exists between decomposition and temperature (Kätterer et al., 1998; Portner et al., 2010). Even when the Q_{10} formulation is chosen, the range of the Q_{10} parameter is large (Segers, 1998). We discuss in section 5 its influence. θ is the dimensionless soil moisture environmental modifier (Figure 2b) given by

$$\theta = \begin{cases} \min\left(0.05, \max\left(1, -1.10\theta^2_{\text{fc}} + 2.4\theta_{\text{fc}} - 0.29\right)\right) & , \forall \theta_{\text{fc}} < 1 \quad (4a) \\ \max\left(0.5, 1 - 0.5\theta_{\text{sat}}\right) & , \forall \theta_{\text{fc}} \geq 1 \quad (4b) \end{cases}$$

θ_{fc} and θ_{sat} are the dimensionless water indexes relative to the field capacity and saturation, computed as follows in each ISBA layer:

$$\theta_{\text{fc}} = \frac{w_g - w_{\text{wilt}}}{w_{\text{fc}} - w_{\text{wilt}}} \quad \forall w_{\text{wilt}} \leq w_g \leq w_{\text{fc}} \tag{5a}$$

$$\theta_{\text{sat}} = \frac{w_g - w_{\text{fc}}}{w_{\text{sat}} - w_{\text{fc}}} \quad \forall w_g > w_{\text{fc}} \tag{5b}$$

where w_g (m^3/m^3) is the volumetric liquid water content in each layer, w_{wilt} (m^3/m^3 is the wilting point corresponding to a matric potential of −15 bars, w_{fc} (m^3/m^3) is the field capacity corresponding to a matric potential of −0.33 bar, and w_{sat} (m^3/m^3) the soil porosity.

Soil decomposition increases with soil water content, as long as the water is not a limiting factor for microbial development. Soil moisture favors microbial activity. However, at high soil water content, diffusion of dioxygen is reduced and limits oxic decomposition by microbes. In the model, decomposition increases with

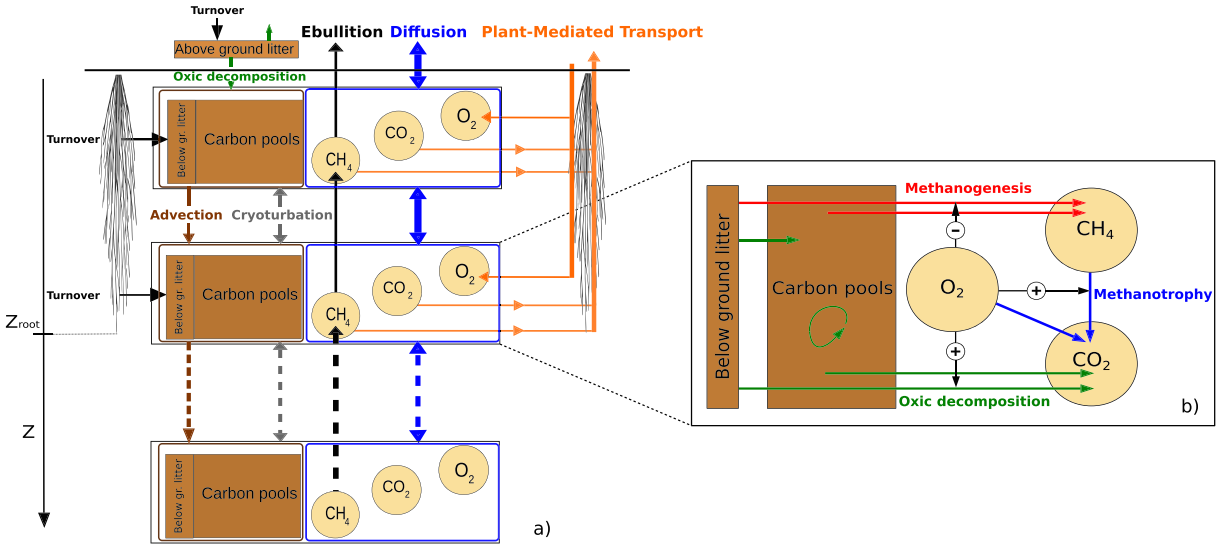

Figure 1. Model schematic with (a) organic matter and gas vertical exchanges between model layers. Each black rectangle represents a model layer. Blue boxes represent the gas pools; brown boxes represent the organic matter reservoirs. Arrows connecting boxes edges represent processes common to all pools inside. (b) Biogeochemical processes inside a model layer: oxic decomposition, methanogenesis, methanotrophy, interactions, and feedbacks between gases and soil organic matter. For the purpose of clarity, the five soil organic carbon and litter pools are not detailed.

the soil water content up to the field capacity w_{fc} (equation (4a)). Above, decomposition decreases linearly down to 0.5 at saturation (equation (4b)).

In the bulk carbon model, moisture and temperature rate specifiers θ and k_i are calculated from the mean temperature and moisture value over the first 10 cm for the two aboveground litter pools and over the first meter of soil for the other pools.

2.1.2. New Soil Carbon Module: Discretization and Methanogenesis

To correctly represent the biogeochemical processes leading to greenhouse gas emissions in high-latitude soils, the model has to simulate the freezing and thawing of the soil and the amount of carbon is affected by the thawing. Hence, we vertically discretized the soil carbon model at the same nodes as the energy and hydrological module of ISBA (Decharme et al., 2013). The environment-specific rate modifier terms k_i and θ are now calculated at each layer. Similarly, the carbon input from root exudates and root decay $S_i(z)$ is now weighted by the root fraction in each layer. The downward transport of carbon, hydrologically induced or due to peat accumulation, is modeled by an advection term as described in Guenet et al. (2013), Koven et al. (2009), and Koven et al. (2013). On permafrost soils, the carbon mixing due to cryoturbation (alternation of thawing and freezing) is modeled as a diffusive process whose diffusion coefficient depends on the active layer depth (Koven et al., 2009). Methanogenesis, detailed in section 2.2.1 and not taken into account in the original model, is now considered as a SOM sink. The vertically discretized soil carbon equation is now written as

$$\frac{\partial C_i(z)}{\partial t} = \frac{\partial}{\partial z}\left[D(z)\frac{\partial C_i(z)}{\partial z}\right] + \frac{\partial A C_i(z)}{\partial z} + S_i(z) + \sum_{j\neq i}\left[(1-r_j)f_{ji}F^j_{\text{oxic}}(z)\right] - F^i_{\text{oxic}}(z) - r_{\text{MG},i}(z)\frac{M_C}{M_{\text{CH}_4}} \quad (6)$$

where z is the depth, $D(z)$ the diffusion coefficient of the cryoturbation (m^2/s) as modeled by Koven et al. (2009), A the advection velocity (m/s) fixed in this work at 2 mm/year to emulate the high carbon content due to peat accumulation in the three sites studied in this work, $r_{\text{MG},i}$ the methane production from pool i (see equation (23)), and M_C and M_{CH4} the molar masses of C and CH_4. Figure 1a represents vertical dynamics of carbon pools and Figure 1b the soil carbon-related processes inside a model layer. Equation (7) is discretized by a Crank-Nicolson semi-implicit scheme, casted in a tridiagnonal system of equations and solved using the tridiagonal matrix algorithm.

As the model computes O_2 concentrations within the soil (section 2.2), we add an explicit limitation for the oxic decomposition by computing the maximum mass of soil carbon C_{max} (gC/m^3) that could react with the

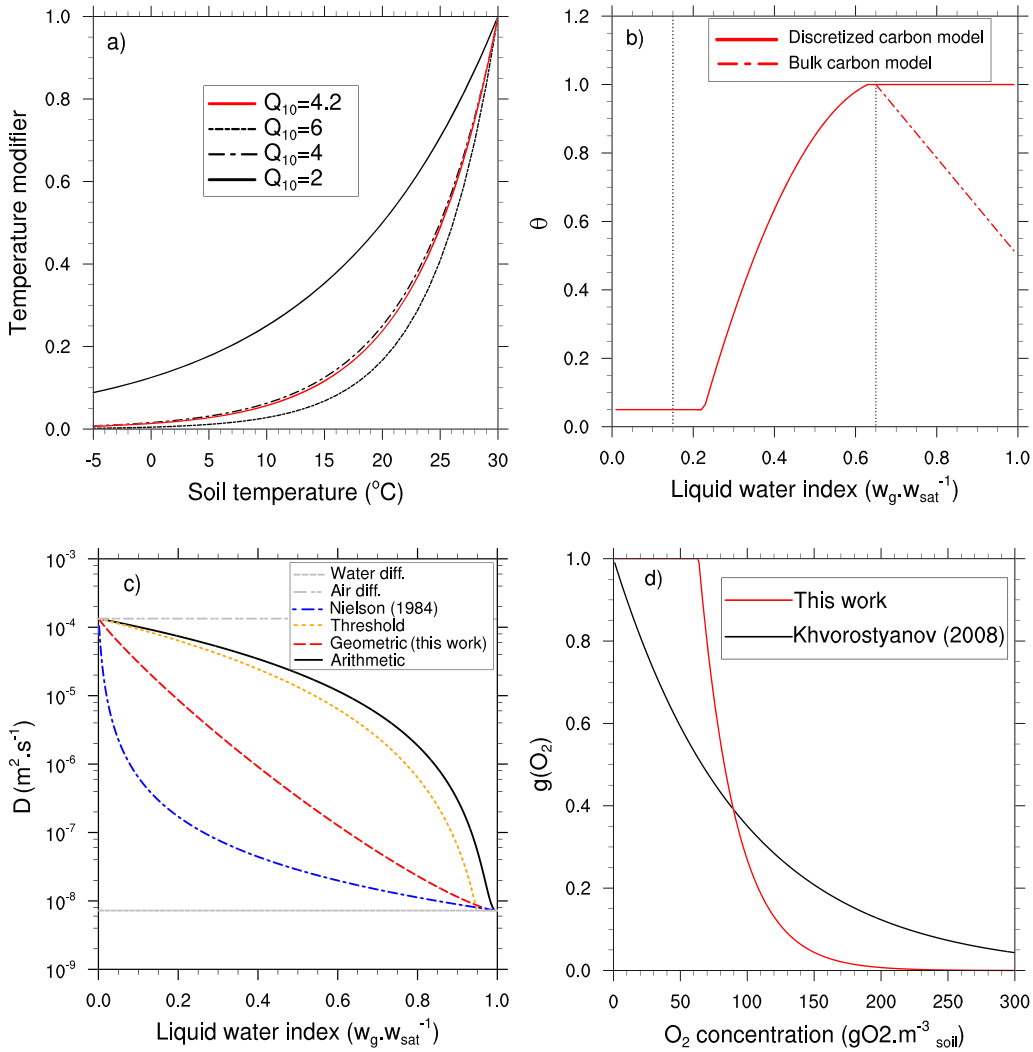

Figure 2. (a) Soil temperature rate modifiers for different Q_{10} values used in this work. (b) Moisture control θ on oxic decomposition for the bulk carbon model and for the discretized carbon model. Vertical dotted lines represent w_{wilt} and w_{fc}. (c) Different bulk diffusivities parametrizations, with no ice content and a Henry's constant of 1 (see Appendix B). (d) Dioxygen dependency function $g(O_2)$ for methanogenesis.

available dioxygen, with a one-to-one ratio (Khvorostyanov et al., 2008)

$$C_{\max}(z) = O_2(z)\epsilon_{O_2}(z)\frac{M_C}{M_{O_2}} \tag{7}$$

with ϵ_{O_2} the total O_2 soil porosity, defined in section 2.2. For every soil carbon pool we limit the decomposition so that the total mass of soil carbon transformed at each time step Δt does not exceed the maximum mass $C_{\max}$

$$F^i_{\text{oxic}}(z) = \theta(z)k_i(z,T_g)C_i(z) \times \min\left(1, \frac{C_{\max}(z)}{\Delta t}\frac{1}{\sum_j \theta(z)k_j(z,T_g)C_j(z)}\right) \tag{8}$$

Taking into account this dioxygen limitation renders the linear decrease of the function θ for w_g values above w_{fc} (equation (4b)) obsolete. The new moisture control function θ is shown in Figure 2b.

In the remainder of the paper, we omit the dependence in z and write all depth-dependent variables $x(z)$ as x.

2.2. Gas Module

In the bulk carbon module, gas created within the soil is released instantaneously into the atmosphere and does not pass through the soil matrix. In a multilayer carbon module, an explicit representation of gas is necessary: gas concentration, and the processes directly impacting it, such as methanotrophy, and gas movement. In addition to CO_2 and CH_4, we calculate O_2-related processes within the soil column, as the O_2 penetration depth determines oxic and anoxic zones, thus separating methane production and methane oxidation (Askaer et al., 2011).

We assume an instantaneous and forced equilibrium between gas concentration within the air-filled part and the water-filled part of the soil in each layer (Khvorostyanov et al., 2008; Tans, 1998; Tang et al., 2013; Tang & Riley, 2014). This assumption allows us to solve the gas vertical diffusion in the soil air and in the soil water using a single state variable. This variable is the gas concentration within the air-filled pores. Within this framework, the prognostic equations for CO_2, CH_4, and O_2 in the gas primary form (Tang & Riley, 2014) can be written as

$$\varepsilon_{CO_2}\frac{\partial [CO_2]}{\partial t} = \frac{\partial}{\partial z}\left(D_{CO_2}\frac{\partial [CO_2]}{\partial z}\right) + r_{oxic} + r_{MT}\frac{M_{CO_2}}{M_{CH_4}} - r^{CO_2}_{PMT} - r^{CO_2}_{transp} \tag{9a}$$

$$\varepsilon_{CH_4}\frac{\partial [CH_4]}{\partial t} = \frac{\partial}{\partial z}\left(D_{CH_4}\frac{\partial [CH_4]}{\partial z}\right) + \frac{\partial \varepsilon_{CH_4} V_e [CH_4]^{ebu}}{\partial z} + \sum_i r_{MG,i} - r_{MT} - r^{CH_4}_{PMT} - r^{CH_4}_{transp} \tag{9b}$$

$$\varepsilon_{O_2}\frac{\partial [O_2]}{\partial t} = \frac{\partial}{\partial z}\left(D_{O_2}\frac{\partial [O_2]}{\partial z}\right) - r_{MT}\frac{M_{O_2}}{M_{CH_4}} - r_{oxic}\frac{M_{CO_2}}{M_{CH_4}} + r^{O_2}_{PMT} - r^{O_2}_{transp} \tag{9c}$$

where $[CO_2]$, $[CH_4]$, and $[O_2]$ are the gas concentrations in the air-filled pores of the soil (g/m^3_{air}). Note that we do not represent ice-trapped gas, a process still missing in current process-based methane models (Xu et al., 2016).

Within the framework of equilibrium between gaseous and aqueous phases, we define the total gas porosity for each gas, that is, the volume available in the air-filled and water-filled fraction of the pores per unit volume of soil

$$\varepsilon_{CO_2} = v + w_g H^{cc}_{CO_2} \tag{10a}$$

$$\varepsilon_{CH_4} = v + w_g H^{cc}_{CH_4} \tag{10b}$$

$$\varepsilon_{O_2} = v + w_g H^{cc}_{O_2} \tag{10c}$$

with v the air fraction (m^3/m^3) computed as

$$v = w_{sat} - w_g - w_{gi} \tag{11}$$

and w_{gi} the volumetric ice content (m^3/m^3).

The ϵs can be thought of as the ratio between the concentration per soil volume and the concentration of air-filled pores. $H^{cc}_{CO_2}$, $H^{cc}_{CH_4}$, and $H^{cc}_{O_2}$ are the dimensionless Henry's solubility constants that determine the ratio between gas phase and aqueous phase concentration of a species (Sander, 2015).

The first term of the right-hand side of equations (9a)–(9c) describes the diffusion of gas through the soil. For methane (equation (9b)), the second term represents ebullition, modeled as a threshold advection term with V_e the bubble velocity (m/s) and $[CH_4]^{ebu}$ the potential methane concentration subject to ebullition. The ebullition algorithm is detailed in section 2.2.4 (equations (30)–(32)). The r terms represent the variations of each gas due to sources, sinks, and transports. The r_{transp} represents the transpiration contribution (equation (17)), r_{oxic} the oxic decomposition (equation (18)), $r_{MG,i}$ the methanogenesis from carbon pool i (equation (23)), r_{MT} the methanotrophy (equation (26)), and r_{PMT} the PMT contribution (equation (29)).

We start by describing the diffusion terms, followed by the sources and sinks, and the model boundary conditions. As many variables and processes are common to several gases, in the rest of this work, we use the notation X to represent CO_2, CH_4, or O_2.

2.1.2. Gas Diffusion

D_X represents the bulk medium diffusion coefficient, computed as the weighted geometric mean of the diffusion coefficients in air D_X^a and in water D_X^w, reduced by the soil permeability in unsaturated and saturated porous media, η_a and η_w, respectively. Bulk medium diffusion is written as

$$D_X = \left(\left(D_X^a \eta_a \right)^{\nu} \times \left(D_X^w H_X^{cc} \eta_w \right)^{w_g} \right)^{\frac{1}{\nu + w_g}} \tag{12}$$

η_a and η_w, also used by Tang et al. (2013), follow Moldrup et al. (2003)

$$\eta_a = \nu \left(\frac{\nu}{w_{\text{sat}}} \right)^{\frac{3}{b}} \tag{13a}$$

$$\eta_w = w_g \left(\frac{w_g}{w_{\text{sat}} - w_{gi}} \right)^{\frac{b}{3-1}} \tag{13b}$$

where b is the Clapp-Hornberger shape parameter (Clapp & Hornberger, 1978).

Many models use an arithmetic mean to compute the bulk diffusivity (e.g., Khvorostyanov et al., 2008; Tang et al., 2013; Tang & Riley, 2014) or a threshold formulation by imposing the water diffusivity for sufficiently high water contents and diffusion in the air (or an arithmetic mean between diffusion in air and water) below that threshold (e.g., Wania et al., 2010). However, bulk diffusivity in soil is very nonlinear with respect to water content (Nielson et al., 1984; Stephen et al., 1998): very little insterstitial water can drastically slow gas diffusion in the soil. By way of analogy with the aggregation methods used for computing thermal and hydrological conductivities (Decharme et al., 2016; Peters-Lidard et al., 1998), we chose a geometric formulation, closer to the observations of Nielson et al. (1984) than actual state-of-the-art formulations. These different bulk diffusivites are shown in Figure 2c and further discussed in Appendix B.

Diffusivities depend on temperature. For diffusivities in air, we use Lerman (1979) formulations

$$D^a_{\text{CO}_2} = \left(0.1325 + 0.00009\, T_g \right) \times 10^{-4} \quad \text{m}^2/\text{s} \tag{14a}$$

$$D^a_{\text{CH}_4} = \left(0.1875 + 0.00013\, T_g \right) \times 10^{-4} \quad \text{m}^2/\text{s} \tag{14b}$$

$$D^a_{\text{O}_2} = \left(0.1759 + 0.00117\, T_g \right) \times 10^{-4} \quad \text{m}^2/\text{s} \tag{14c}$$

For diffusivities in water, we use the parametrization of Broecker and Peng (1974), also used by Wania et al. (2010)

$$D^w_{\text{CO}_2} = \left(0.939 + 0.002671\, T_g + 0.0004095\, {T_g}^2 \right) \times 10^{-9} \quad \text{m}^2/\text{s} \tag{15a}$$

$$D^w_{\text{CH}_4} = \left(0.9798 + 0.002986\, T_g + 0.0004381\, {T_g}^2 \right) \times 10^{-9} \quad \text{m}^2/\text{s} \tag{15b}$$

$$D^w_{\text{O}_2} = \left(1.172 + 0.03443\, T_g + 0.0005048\, {T_g}^2 \right) \times 10^{-9} \quad \text{m}^2/\text{s} \tag{15c}$$

The dimensionless Henry's solubility H_X^{cc} is also temperature dependent, and by assuming the ideal gas law, we have for each gas

$$H_X^{cc} = H_X^{cp} \times RT = B_X \frac{T_K}{T_{\text{stp}}} \tag{16}$$

where T_K is the temperature in K, $T_{\text{stp}} = 273.15$ K, H_X^{cp} the Henry solubility ($\text{mol} \cdot \text{m}^{-3} \cdot \text{Pa}$), R the universal gas constant, and B_X the dimensionless Bunsen coefficient. We used the most recent values given in Sander (2015): $B_{\text{CH}_4} = 0.0318$, $B_{\text{CO}_2} = 0.749$, and $B_{\text{O}_2} = 0.0296$.

2.1.2. Transport, Sources, and Sinks

In the model, all gases are affected by diffusion (upward and downward transport), PMT (upward for CO_2 and CH_4 and downward for O_2) and transpiration (upward). In this version of the model, only methane is affected by ebullition (see section 5). Figure 1a represents the schematic of the vertical transport of gases. PMT and ebullition are further detailed in section 2.2.4.

The water extracted by plants through transpiration carries dissolved gas (Riley et al., 2011). We represent the transport of gas via transpiration, layer by layer

$$r^{X}_{\text{transp}} = \frac{F_{\text{transp}} H^{cc}_{X} [X]}{\rho_w} \tag{17}$$

where F_{transp} ($\text{kg}\cdot\text{m}^{-3}\cdot\text{s}^{-1}$) is the amount of water transported by transpiration and ρ_w (kg/m^3) the volumic mass of water.

Within the soil, the CO_2-related processes involve two net sources. The first source is the oxic decomposition of the belowground carbon and litter pools r_{oxic} ($\text{gCO}_2\cdot\text{m}^{-3}_{\text{soil}}\cdot\text{s}^{-1}$), defined in equation (8)

$$r_{oxic} = \sum_i F^i_{\text{oxic}} r_i \frac{M_{\text{CO}_2}}{M_C} \tag{18}$$

The CO_2 produced by the decomposition of the aboveground litter pool is released directly into the atmosphere and does not pass through the soil CO_2 pool. The other source is the CO_2 produced by methanotrophy (see equation (26)), simplified here as

$$\text{CH}_4 + 2\text{O}_2 \rightarrow \text{CO}_2 + 2\text{H}_2\text{O} \tag{19}$$

There are no sources of O_2 within the soil, and the O_2 is consumed by oxic decomposition and methanotrophy.

There is one source of CH_4 within the soil, methanogenesis r_{MG}, and one sink, methanotrophy r_{MT}. These terms are described in detail in section 2.2.4.

2.1.2. Numerical Method and Boundary Conditions

For each gas, all processes in equations (9a)–(9c) are treated at once, unlike several other models that treat methanogenesis, methanotrophy, diffusion, PMT, and ebullition sequentially. The set of equations is discretized by a Crank-Nicholson semi-implicit scheme and cast as a tridiagonal system of equations. A time splitting option is also implemented for large time steps.

At the deepest soil layer we impose a no-flux boundary condition for all gases

$$\left.\frac{\partial [X]}{\partial z}\right|_{z=z_{\max}} = 0 \tag{20}$$

At the soil-atmosphere interface, we impose the following boundary condition:

$$\left[\text{CH}_4\right]\Big|_{z=0^+} = \frac{p_s}{RT_s} \text{CH}_{4s} M_{\text{CH}_4} \tag{21}$$

where p_s is the atmospheric surface pressure, T_s the atmospheric surface temperature, R the universal gas constant, and CH_{4s} the methane mixing ratio fixed at 1.7 ppm.

A similar boundary condition is imposed for O_2, with the observed mixing ratio of 20.9%. For CO_2, the observed global atmospheric CO_2 concentration is used (NOAA/ESRL—www.esrl.noaa.gov/gmd/ccgg/trends/).

Finally, arctic snowpack including iced layers suppresses soil-atmosphere gas exchanges, leading to CO_2 and CH_4 accumulation in the snowpack (Pirk et al., 2016). Since we do not explicitely represent gases in the snowpack, we model this effect by reducing the diffusivity at the interface between the atmosphere and the first soil layer by a snow dependence function g_{snow}

$$g_{\text{snow}} = f_{\text{snow}} \left(1 - \frac{\rho_{\text{snow}}}{\rho_{\text{ice}}}\right) + \left(1 - f_{\text{snow}}\right) \tag{22}$$

where f_{snow} is the grid cell fraction covered by snow, ρ_{snow} the density of the snow layer closest to the ground, and ρ_{ice} the density of ice.

2.2.1. Methane Processes

A common method for distinguishing methane production and oxidation zones is to diagnose a priori the water table level and to force methanogenesis to occur only below this level and methanotrophy only above (e.g., Kaiser et al., 2016; Walter & Heimann, 2000; Zhu et al., 2014). This classical strata approach has recently been criticized (Yang et al., 2017). As we compute the O_2 concentration within the soil column, we can calculate directly where anoxic conditions occur within the model and we do not need to use the water table in the methane model equations, as shown in Figure 1.

Methanogenesis takes place in the water-filled pores when O_2 concentration is low enough, whereas methanotrophy occurs in aerobic conditions. Once CH_4 is created within the soil column, it can escape the soil matrix via diffusion in the water and air-filled pores; ebullition, only in the water-filled pores; PMT through aerenchyma; and transpiration (equation (17)).

2.2.1.1. Methanogenesis

Methane is produced by methanogens, which are anaerobic archea (Stams & Plugge, 2003). The main environmental factors controlling the rate of methane production are (1) the availability and quality of suitable organic matter, (2) temperature, (3) soil moisture, and (4) dioxygen content, all of which are calculated by the model in every soil layer. The carbon pool available for methanogenic archaea consists mainly of root exudates and labile plant material that can be easily degraded (Chanton et al., 1995). In arctic regions, this material is not necessarily recent due to the cold conditions that prevent decomposition (Mueller et al., 2015). In the model, carbon pools impacted by methanogenesis are the belowground litter pools $C_{bg,[s,m]}$ and the active carbon pool C_a. For each of these reservoirs, the characteristic time for decomposition by methanogenesis is 10 times the characteristic time for oxic decomposition (Khvorostyanov et al., 2008; Table 1). We use the same Q_{10} temperature function as for the oxic decomposition (equation (3)) because it is in the range observed by Segers (1998) in minerotrophic peats. Hence, the rate of methanogenesis is the oxic decomposition rate divided by 10. The methanogenesis from pool i per soil volume $r_{\mathrm{MG},i}(z,t)$ ($\mathrm{gCH_4 \cdot m^{-3}_{soil} \cdot s^{-1}}$) is given by

$$r_{\mathrm{MG},i} = \delta_i C_i \frac{w_g}{w_{\mathrm{sat}}} \frac{k_i(T_g)}{10} f\left(T_g\right) g\left(O_2\right) \frac{M_{\mathrm{CH_4}}}{M_C} \tag{23}$$

where i designates the type of carbon pool defined in Table 1, $\delta_i = 1$ when $i = a$ or $i = bg,[s,m]$ and 0 otherwise. $g(O_2)$ is the dioxygen dependency function. $f(T_g)$ is a function that ensures that methanogens are not active at subzero temperature because the Q_{10} function decreases too slowly below 0 °C (Figure 2a). Indeed, recent incubations results (Treat et al., 2014) show almost no methane fluxes below 0 °C. We impose a linear decrease between 0 and $T_{lim} = 1$ °C

$$f\left(T_g\right) = \begin{cases} 1, & T_g \geq T_{lim} \\ \frac{T_g}{T_{lim}}, & 0°C \leq T_g \leq T_{lim} \\ 0, & T_g \leq 0°C \end{cases} \tag{24}$$

O_2 strongly inhibits methanogenesis (Askaer et al., 2011), and we parametrize this dependency as follows:

$$g\left(\mathrm{O_2}\right) = \frac{10^{\left(\mathrm{O_{2,lim}} - [\mathrm{O_2}]H^{cc}_{\mathrm{O_2}}\right)/\mathrm{O_{2,lim}}} - 10^{(\mathrm{O_{2,lim}}-10)/\mathrm{O_{2,lim}}}}{1 - 10^{(\mathrm{O_{2,lim}}-10)/\mathrm{O_{2,lim}}}} \tag{25}$$

where $O_{2,lim}$ is the aqueous phase threshold dioxygen concentration (Duval & Goodwin, 2000), fixed in this work at 2 $\mathrm{gO_2/m^3_{water}}$, roughly equivalent to 60 $\mathrm{gO_2/m^3_{air}}$ in standard pressure and temperature conditions. Khvorostyanov et al. (2008) also used a O_2 formulation to constrain methanogenesis. We did not choose their function as it implies methane production at high oxygen content (Figure 2d), and although methanogens can still survive in aerated soils (Angel et al., 2011), they are strict anaerobes and methanogenesis is fully suppressed upon exposure to dioxygen (Yuan et al., 2009).

2.2.1.2. Methanotrophy

Methane can be oxidized by methanotrophic bacteria, in aerobic parts of the soil. Unlike some state-of-the art models that use a Michaelis-Menten equation—presented later—without a temperature dependency to describe the methanotrophy reactions, we propose to represent methanotrophy as an exponential decay of methane concentration (i.e., a first-order differential equation), constrained by temperature and O_2

Table 2
Short Review of Parameters Used in Soil Methanotrophy Modeling

Reference	K_{CH_4} (mol/m^3)	V_{max} (mol·m^{-3} · s^{-1})	$\tau_{MT}(t)$
	Michaelis-Menten framework		
Riley et al. (2011)	5×10^{-4} to -5×10^{-2}	1.25×10^{-6} to 1.25×10^{-4}	—
Tang et al. (2010)	0.44	10^{-8} to 10^{-7}	—
Raivonen et al. (2017)	0.44	2.7×10^{-4}	—
Walter and Heimann (2000)	0.016–0.08	2×10^{-6} to 2×10^{-5}	—
	First-order kinetic framework		
Jørgensen et al. (2015)[a]	—	—	1.4 hr
Murguia-Flores et al. (2017)	—	—	5.5 hr
Khvorostyanov et al. (2008)	—	—	5 days

[a]From incubation experiments.

concentration. The amount of methane consumed by methanotrophy per soil volume ($gCH_4 \cdot m_{soil}^{-3} \cdot s^{-1}$) is written as

$$r_{MT} = \epsilon_{CH_4} CH_4 k_{MT}(T_g) \frac{[O_2]}{K_{O_2} M_{O_2} + [O_2]} \tag{26}$$

where $k_{MT}(T_g)$ (s^{-1}) is the methanotrophy time-dependant rate, inferred from incubation experiments of Jørgensen et al. (2015)

$$k_{MT}\left(T_g\right) = \frac{1}{\tau_{MT}} \times 4.2^{\frac{T-18.7}{10}} \tag{27}$$

and τ_{MT} (s) the time constant of the methanotrophy. τ_{MT} is chosen as 1 day, which is a median of the values found in literature (Table 2). We take into account the dioxygen limitation by using a Michaelis-Menten kinetic with K_{O_2} fixed at 2 mol/m^3 following Kaiser et al. (2016).

In their pioneering process-based works, Walter et al. (1996) modeled the methane oxidation with a Michaelis-Menten equation

$$r_{MT}\big|_{\text{Michaelis-Menten}} = \frac{V_{max} \quad [CH_4]}{K_{CH_4} + [CH_4]} \tag{28}$$

where V_{max} (mol·m^{-3}·s^{-1}) is the potential methane oxidation rate and K_{CH_4} (mol/m^3) the Michaelis-Menten constant. This formulation has been widely used in the soil methane modeling community (Arah & Stephen, 1998; Kaiser et al., 2016; Riley et al., 2011; Zhu et al., 2014). Segers (1998) noted in his review that V_{max} values range from 10^{-4} to 10^{-7} mol·m^{-3}·s^{-1}. From one model to another, the choice of V_{max} and K_{CH_4} vary by several orders of magnitude, as shown in Table 2. Hence, for the same methane concentration, methanotrophy characteristic times vary from a few hours to several days.

Wania et al. (2010) do not use a Michaelis-Menten model for methanotrophy, but consider that a fixed fraction of available dioxygen is used to oxidize available methane directly, with a stochiometry balance of two moles of dioxygen for each mole of oxidized methane.

In the Michaelis-Menten equation behavior, if methane concentration strongly exceeds K_{CH_4}, the model tends to a zero-order kinetic, that is, a constant methane consumption, independent of methane concentration. Inversely, if the methane concentration is much lower than K_{CH_4}, model tends to a first-order kinetic, that is, a classical exponential decay. In Walter and Heimann (2000), soil methane concentration exceeds K_{CH_4} and methanotrophy as defined in equation (28) is reduced to a zero-order kinetic. But recent works in Greenland suggest the opposite. In the supporting information of Jørgensen et al. (2015), field studies in the Zackenberg valley and incubation experiment results clearly suggest a first-order kinetic reaction. Moreover, these results clearly show a strong temperature dependency that some present-day models do not consider, with the exception of Riley et al. (2011). Computing these rates from supporting information Figure S3a of Jørgensen et al. (2015), we find rates ranging from 17 to 1.8 day^{-1} when temperatures goes from 18.7 to 2.9 °C. These dynamics corresponds to a Q_{10} value of 4.2 (Figure 2a). Those methanotrophy rates are much higher than the one chosen by Khvorostyanov et al. (2008), that is, 0.2 day^{-1}.

Finally, from a modeling point of view, one can question the use of the Michaelis-Menten kinetic, which requires two parameters, both highly uncertain (Segers, 1998; Table 2) to choose and tune, instead of a simpler first-order ordinary differential equation, as used, for instance, by the global soil methanotrophy model MeMo (Murguia-Flores et al., 2017) or Khvorostyanov et al. (2008).

2.2.1.3. Plant-Mediated Transport and Aerenchyma

Wetland plants have adapted to the permanently waterlogged conditions by developing air-filled channels called aerenchyma in their shoots and roots (Schlesinger & Bernhardt, 2013). These channels deliver O_2 from the surface to the roots but allow also direct transport of CH_4 and CO_2 from the soil to the atmosphere. This was first modeled by Walter et al. (1996) as a direct uptake from the soil to the atmosphere, weighted by a function of the leaf area index (LAI) and empirical parameters describing the "strength" of such transport. In more recent works (Kaiser et al., 2016; Riley et al., 2011; Raivonen et al., 2017; Wania, 2007), the consensus is to take into account the concentration gradient between the atmosphere and gas in the soil column but with various complexity levels to represent the transport through the soil. The most complex formulations (Kaiser et al., 2016; Wania, 2007) explicitly model roots using concepts like root diameters, tiller density and tiller porosity, or aerenchyma exodermis thickness (Kaiser et al., 2016). These parameters are not well known and vary broadly not only from one species to another (Colmer, 2003; Schimel, 1995) but also within a single species due to substantial small-scale spatial variations (Kutzbach et al., 2004). Moreover, among different plant species, a greater PMT capacity does not necessarily correlate with higher total emissions (Bhullar et al., 2013). To be consistent with the overall complexity of the carbon and vegetation model, we choose a simpler representation.

In our model, the flux of methane transported by roots and plants for a layer j $f_{\mathrm{PMT}}^{\mathrm{CH_4},j}$ ($\mathrm{gCH_4 \cdot m_{soil}^{-2} \cdot s^{-1}}$) is inspired by Riley et al. (2011) and defined by

$$f_{\mathrm{PMT}}^{\mathrm{CH_4},j} = \frac{\epsilon_{\mathrm{CH_4}} \Pi_a \alpha_{\mathrm{CH_4}} \left(\left[\mathrm{CH_4}\right] - \left[\mathrm{CH_4}\right]_{\mathrm{atmo}} \right)}{r_a + \frac{r_L \times z_j + 0.5 h_{\mathrm{plant}}}{D_{\mathrm{CH_4}}^a}} \rho_r f_{\mathrm{root}}^j h(\mathrm{LAI}) f_{\mathrm{veg}} \tag{29}$$

The denominator represents the vertical transport velocity of gases through the aerenchyma, with an inner diffusivity equal to that of air. r_a (s/m) is the aerodynamic resistance. The root fraction in the layer j, f_{root}^j, and r_L the ratio of root length to depth, fixed at 3, takes into account the geometry of the roots and the respective contribution of each model layer in the total transport. z_j is the depth of the layer j. As CO_2 and CH_4 (O_2) do not leave (enter) aerenchyma directly at the soil/atmosphere interface but through the plant shoot, we take into account the plant height h_{plant} in the transport, approximated by $\frac{\mathrm{LAI}}{6}$.

Radial transport between the root and the soil is representend by the parameter Π_a, corresponding to the aerenchyma permeability. In this work, Π_a is fixed to 1, representing a perfectly permeable tissue. The utilization of gas by the plant during the transport is represented by the parameter α_X. For CH_4 and CO_2, $\alpha_{\mathrm{CH_4}} = \alpha_{\mathrm{CO_2}} = 1$ represents no gas utilization by the plant. For O_2, we fix $\alpha_{\mathrm{O_2}} = 0.3$ as most of the O_2 transported by aerenchyma is used by plant roots and only a fraction is lost to the soil (Colmer, 2003). This attenuation is also coherent with Nielsen et al. (2017) who noted that aerenchymous transport of dioxygen is inefficient compared to the transport of methane.

The strength of the PMT varies in time with the LAI, and following Walter and Heimann (2000), we define a LAI dependency function $h(\mathrm{LAI}) = \min(\frac{\mathrm{LAI\text{-}LAI_{min}}}{2-\mathrm{LAI_{min}}}, 1)$. Finally, f_{veg} is the soil vegetated fraction and ρ_r the aerenchyma inner porosity fixed at 0.3 (Riley et al., 2011). A similar equation stands for CO_2. For O_2, equation (29) is treated as a flux from the atmosphere to the ground.

As we do not explicitly compute gas concentrations inside the roots and aerenchyma, the total plant-mediated flux F_{PMT}^X ($\mathrm{gX \cdot m^{-2} \cdot s^{-1}}$) is computed as the sum of the contribution from all soil layers down to the rooting depth z_{root}. From a *numerical point of view*, the PMT acts as a *sink* for CH_4 and CO_2 and as a *source* for O_2 since gas is not transported between individual layers. Note also that in equations (9a)–(9c) we have $r_{\mathrm{PMT}}^X(t,z) = \frac{f_{\mathrm{PMT}}^{X,j}}{\Delta z_j}$ ($\mathrm{gX \cdot m^{-2} \cdot s^{-1}}$), with Δz_j the thickness of the jth soil layer (m).

2.2.1.4. Ebullition

Unlike most models that consider an instantaneous transport to the atmosphere or to the unsaturated part of the soil regardless the depth at which the bubble is formed, we model ebullition as an advective layer-by-layer transport that takes place in the water-filled pores. The transported methane $\left[\mathrm{CH_4}\right]^{\mathrm{ebu}}$ is the excess of CH_4

with respect to a concentration threshold X_{ebu}, depending on environmental variables. We trigger ebullition when the soil water content is high enough

$$X_{ebu} = \frac{r_{CH_4} P_s M_{CH_4}}{RT_g} \tag{30}$$

$$[CH_4]^{ebu} = \begin{cases} [CH_4] - X_{ebu}, & \text{if } [CH_4] \geq X_{ebu} \text{ and } w_g \geq 0.9 \times (w_{sat} - w_{gi}) \\ 0, & \text{otherwise} \end{cases} \tag{31}$$

where P_s is the soil pressure (i.e., the sum of hydrostatic and atmospheric pressure, as the latter plays a role in triggering ebullition events; Tokida et al., 2007), R the gas constant, and r_{CH_4} the saturated mixing ratio of CH_4, fixed at 15% (Riley et al., 2011). This threshold may depend on vegetation, but it is still unclear in which way. Grünfeld and Brix (1999) noted that ebullition is dominant in nonvegetated plots, but Walter and Heimann (2000) model the opposite, considering that N_2 concentrations are higher in vegetated soils, hence increasing condensation nuclei numbers. We chose not to take vegetation into account.

Numerically, in order to maintain the tridiagonal structure of the Crank-Nicholson solver, we had to ensure that a bubble does not travel through more than two soil layers within the same time step. Hence, the velocity of bubbles in each layer j, noted V_e^j (m/s), depends on the thickness of the considered layer, on the model time step and on the soil tortuosity η, fixed here at 0.66

$$V_e^j = \frac{\Delta z_j}{\Delta t} \eta \tag{32}$$

The velocity of the first soil layer is weighted by the snow dependence function $g_{snow}(t)$, in the same way as the diffusion coefficient at the soil-atmosphere interface: $V_1 = \frac{\Delta z_1}{\Delta t} \eta . g_{snow}$.

Finally, the ebullition flux going into the atmosphere is computed as the bubbles leaving the top layer. By choosing this layer-by-layer formulation, the ebullition flux could be 0 because the water and methane conditions (equation (31)) are not fulfilled in the top layer, while ebullition is still occurring in some subsurface layers. Note also that this formulation allows methane transported by ebullition in the deepest layers to be later impacted by other processes, such as methanotrophy.

3. Site Description, Material, and Methods

We evaluate this model against observations from three arctic wetland sites: one without permafrost (Nuuk) and two (Zackenberg and Chokurdakh) on permafrost soils. The Nuuk and Zackenberg sites are both part of the Greenland Ecosystem Monitoring program, which provides detailed reports on an annual bases, dating back to 2007 for Nuuk (Nuuk Ecological Research Operations-NERO-Annual reports; Tamstorf et al., 2008) and 1995 for the Zackenberg site (Zackenberg Ecological Research Operations-ZERO-Annual reports; Meltofte & Thing, 1996).

At Nuuk and Zackenberg, CH_4 and CO_2 fluxes data come from several automatic closed chambers (6–10) and we use the mean of these chamber fluxes. When more than one automatic chamber is active, the standard deviation between the active automatic chambers is provided. The number of functioning chambers varies in time. There is a large spatial variability of methane fluxes between individual automatic chambers, even though they are relatively close together (a few meters), as shown in Pirk et al. (2017) on the Nuuk and Zackenberg sites (Skov, 2014). Similar large variations of methane fluxes over a small spatial scale have also been observed by Kutzbach et al. (2004) in northern Siberia. At Chokurdakh, CH_4 data are more sporadic, as they come from manual closed chambers. The standard deviation of methane fluxes is not available, and we do not have CO_2 chamber data.

3.1. Nuuk

The Nuuk research station is situated in Kobbefjord (64°07′N; 51°21′W), approximately 20 km from Nuuk. Its study area consists of a drainage basin with an area of 32 km^2 situated at the head of a fjord. The local climate is low arctic, with a mean annual temperature of −1.4 °C and mean annual precipitation of 752 mm (1961–1990). Despite cold winter temperatures, the fen never freezes at depth below 10–15 cm. NERO annual reports (Tamstorf et al., 2008) show a significant variability in soil texture, soil moisture, and vegetation. In the model we impose the soil texture measured from a location closest to the automatic chambers

Table 3
Site's Main Characteristics and Data Used for Validation

	Nuuk	Zackenberg	Chokurdakh
	Characteristics		
Longitude-latitude	51.3°W, 66.1°N	21°00′ W, 74°30′N	147.49°W, 70.82°N
Permafrost	No	Yes	Yes
Climate forcing data period	2009–2014	1996–2015	2003–2014
CH_4 fluxes data period	2009–2014	2006–2015	2008–2013
Clay fraction (%)	4.3	14.5	15.0
Sand fraction (%)	91.3	16.7	30.0
Rooting depth (m)	0.3	0.3	0.3
Organic layer depth (m)[a]	0.3	0.4	0.1
Forced water table	0.2m	0.1m	0.1 m
	Data		
CH_4 flux (chambers)	Automatic	Automatic	Manual
CO_2 flux (chambers)	Automatic	Automatic	—
Soil temperatures	Probes	Probes	Probes
Active layer thickness	No permafrost	Manual	—
Latent heat	Eddy tower	Eddy tower	Eddy tower
Sensible heat	Eddy tower	Eddy tower	Eddy tower
Net radiation	Eddy tower	Eddy tower	Eddy tower
Snow depth	Camera	Camera	—

[a]Depth below which organic matter fraction is lower than 70%.

(plot Mart-2; Raundrup et al., 2010). These soil texture samples are taken from the upper 10 cm and do not change much with depth. The automatic chambers are located in a fen at the bottom of a valley surrounded by high rocks. A peat layer of approximately 20–40 cm overlays sedimental, mineral soil layers. Due to its topographic specificity, the main input of water on this site is not from the local precipitation, but from snowmelt and runoff from adjacent hills and inflow from a nearby stream located at the southern border of the fen. One key factor of this site appears to be the snowmelt date, as snow melt water runs through the fen, leading to a saturated fen during the growing season.

3.2. Zackenberg

The Zackenberg site is a permafrost fen located in the Zackenberg valley, in the Northeast Greenland National Park (74°30′N, 21°00′W). It is located in the high Arctic (Meltofte & Rasch, 2008) with mean annual temperature of −9°C. Monthly mean air temperatures are below −20°C in winther and between +3 and +7 °C in summer (Hansen et al., 2008). Zackenberg research station exhibits a large variability of soils and vegetation (Palmtag et al., 2015). The automatic chambers are located in a fen, near the ZK3-2 plot from Palmtag et al. (2015), where sand and clay profiles up to a depth of 80 cm are available. Mineral texture values provided in Table 3 for this site are the mean over the profile, as they do not change much with depth. Even inside the fen land cover class of the Zackenberg valley, many disparities exists in organic content and organic layer depth (Palmtag et al., 2015). There is standing water during the growing season, and the water table level fluctuates from a few centimeters below ground to above the surface (Mastepanov et al., 2013).

3.3. Chokurdakh

The Chokurdakh Scientific Tundra Station (70°49′28”N, 147°29′23”E; elevation 11 m a.s.l.) is situated in the Kytalyk Wildlife Reserve, Northeastern Yakutia, in the lowlands of the Indigarka river in northeast Siberia. This is the coldest of the three studied sites, with a mean annual temperature of −10.5 °C. In January, the monthly mean temperature is −34.2 °C with occasional minima below −40 °C (van der Molen et al., 2007). Mineral soil textures from the Harmonized World Soil Database (FAO et al., 2012) are 30% sand, 15% clay, and 65% silt. These values are consistent with the description found in Parmentier et al. (2011) and van der Molen et al. (2007), where the soil is described mainly as a 10- to 15-cm organic top peat layer overlying silt.

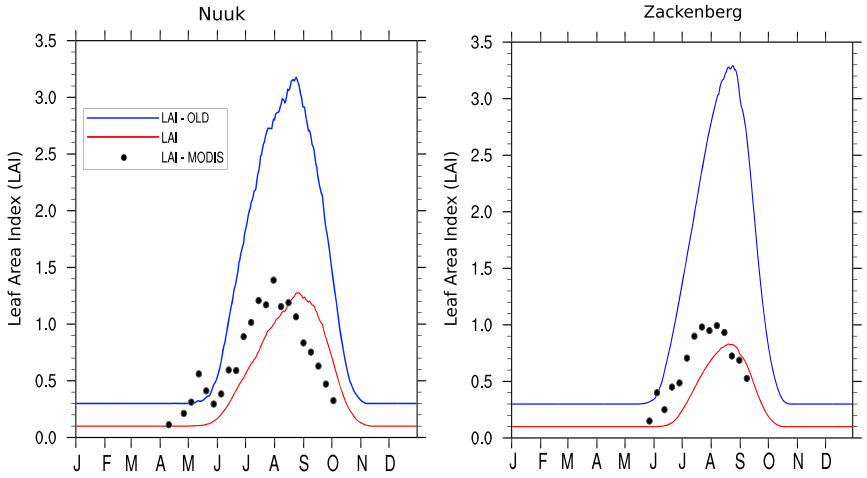

Figure 3. Mean annual cycle of the daily leaf area index (LAI) on Nuuk and Zackenberg site for the full experiment period. Data are from the MODIS Land Product subset tool ORNL DAAC. 2017.

3.4. Experimental Protocol

At each site, we ran the model offline forced by the available hourly atmospheric measurements: air temperature, air moisture, precipitation, and wind speed, short and longwave downward radiation. At Zackenberg, the observed snowfall rate is not consistent with the observed variations in snow depth over the fen. This could lead to important errors in the simulation of the timing of the snowmelt, which is crucial for the CO_2 and CH_4 fluxes. To avoid these discrepancies, we derived the snowfall rate from the positive variations of the observed snow depth.

The model simulation went through an initial 1,500-year spin-up period by cycling the few years of atmospheric forcing in order to achieve equilibrium of the litter pools and the active and slow carbon pools. Due to its very long turnover time, the passive carbon pool contribution to CO_2 fluxes is negligible. At Zackenberg, we used only the first 10 years of the available forcing files to achieve the 1,500-years spin-up, because the last years show a significant positive trend.

The effects of soil organic carbon on soil hydraulic and thermal properties (Decharme et al., 2016) are taken into account by imposing an organic soil fraction profile at each site. Profiles were inferred from organic peat layer depths at each site. In the peat layers, a high soil organic fraction is imposed (≥ 0.7). Due to the lack of data below this peat layer, a parametrization of the decrease in soil organic fraction was done to match at best the observed temperatures (Table 3).

At the three sites, the saturated soil is the result of some microtopographic features and cannot be simulated solely by a local hydrological balance. At Zackenberg, the water table level and the overall moisture are important, with episodes of standing water above the surface—except in 2010—(Mastepanov et al., 2013), and we therefore impose saturation below 10 cm. The same condition is imposed at Chokurdakh. The fen area at Nuuk is in a small depression, and automatic chambers are located near the border of the fen (Pirk et al., 2016), where mean moisture conditions are lower than at Zackenberg. At Nuuk, saturation below 20 cm is imposed. Above these levels, the hydrological model runs free. Model sensitivity to water table level is discussed in section 5. Site-specific parameters, available data, and observation period are shown in Table 3. Finally, as CH_4 fluxes are measured by closed chambers, we do not take into account the role of the aerodynamic resistance r_a (equation (29)).

Three skill scores are used to compare model results to the observations: the daily bias, the sample Pearson correlation coefficient (r), and the centered root-mean-square error (c-rmse). The latter is computed by subtracting for each data set their mean before computing a standard root mean square error. All these skills are computed on the full time series of daily mean data when not stated otherwise. When data are not available, corresponding model results are not taken into account in the skill scores and in the figures presenting mean annual cycles of daily variables, except stated otherwise. When data are missing entirely, model results are shown for the full period of the experiment.

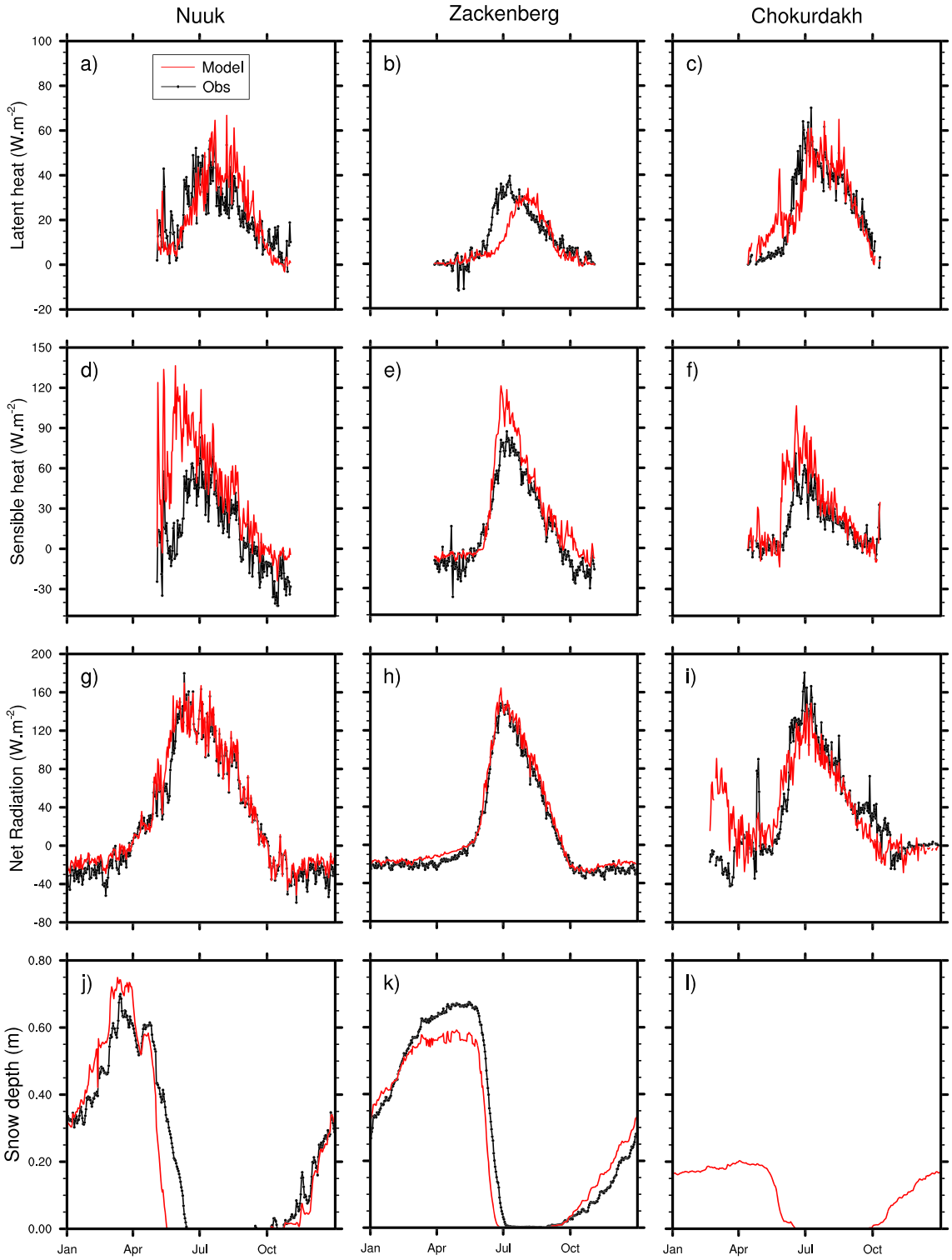

Figure 4. Mean annual cycles of daily latent heat, sensible heat, net radiation, and snow depth on Nuuk (a, d, g, j), Zackenberg (b, e, h, k), and Chokurdakh (c, f, i, l). At Chokurdakh panel (l), snow depth data are missing.

Table 4
Daily Skill Scores for Radiative and Turbulent Fluxes, Snow Depth, and CO_2 and CH_4 Fluxes

			Nuuk	Zackenberg	Chokurdakh
LE (W/m^2)		*n*	681	1,901	1,112
		Mean	23.44	17.36	32.04
		r	0.64	0.55	0.65
		c-rmse	16.07	15.93	19.24
		Bias	2.45	−1.92	−1.5
H (W/m^2)		*n*	743	1,943	1169
		Mean	17.13	30.96	20.96
		r	0.80	0.84	0.47
		c-rmse	26.68	29.17	44.86
		Bias	23.89	17.10	17.16
RN (W/m^2)		*n*	1810	6,288	1727
		Mean	25.85	10.71	64.43
		r	0.95	0.93	0.87
		c-rmse	20.28	22.13	37.1
		Bias	6.41	8.17	−3.6
Snow depth (m)		*n*	1598	6250	—
		Mean	0.24	0.27	—
		r	0.85	0.94	—
		c-rmse	0.18	0.12	—
		Bias	−0.01	−0.01	—
CH_4 flux ($mgCH_4 \cdot m^2 \cdot s^{-1}$)		*n*	505	723 (685)	117
		Mean	3.12	1.50 (0.93)	1.33
		r	0.45	0.18 (0.74)	0.37
		c-rmse	1.9	2.18 (0.79)	1.04
		Bias	0.96	−0.40 (0.22)	0.13
CO_2 flux ($mgCO \cdot m^2 \cdot s^{-1}$)		*n*	416	704 (666)	—
		Mean	−62.6	−8.02 (−73.6)	—
	Old model	r	0.82	0.64 (0.92)	—
		c-rmse	145.2	230.1 (123.2)	—
		Bias	−39.2	−58.4 (−12.1)	—
	New model	*r*	0.75	0.62 (0.86)	—
		c-rmse	130	231.8 (124.0)	—
		Bias	−36.5	−85.8 (−37)	—

Note. For CO_2, results from the old bulk carbon model are also given. The number of day with non missing data (*n*), observed mean, correlation (r), centered root-mean-square error (c-rmse), and bias are shown. Zackenberg skills in brackets (-) are computed without the late-season burst of 2007 and 2009. c-rmse = centered root-mean-square error.

4. Results

After briefly presenting the LAI parameterization, we evaluate the model's ability to reproduce the radiative and turbulent fluxes, the snow depth, the soil temperature, and the active layer thickness. We then analyze the simulated CO_2 and CH_4 fluxes.

4.1. LAI

We first modified the standard LAI parameterization. Indeed, the LAI simulated by the standard version of ISBA for boreal grasses was largely overestimated, peaking at approximately 3.5, while the MODIS/Terra+Aqua LAI product (Myneni & Park, 2015) shows values not exceeding 1.5 at Nuuk and Zackenberg (Figure 3). Using observations from arctic plant communities published by van Wijk et al. (2005), we deduced a specific leaf area of 8 m^2/kg versus 14 in the standard version. The minimum LAI imposed by

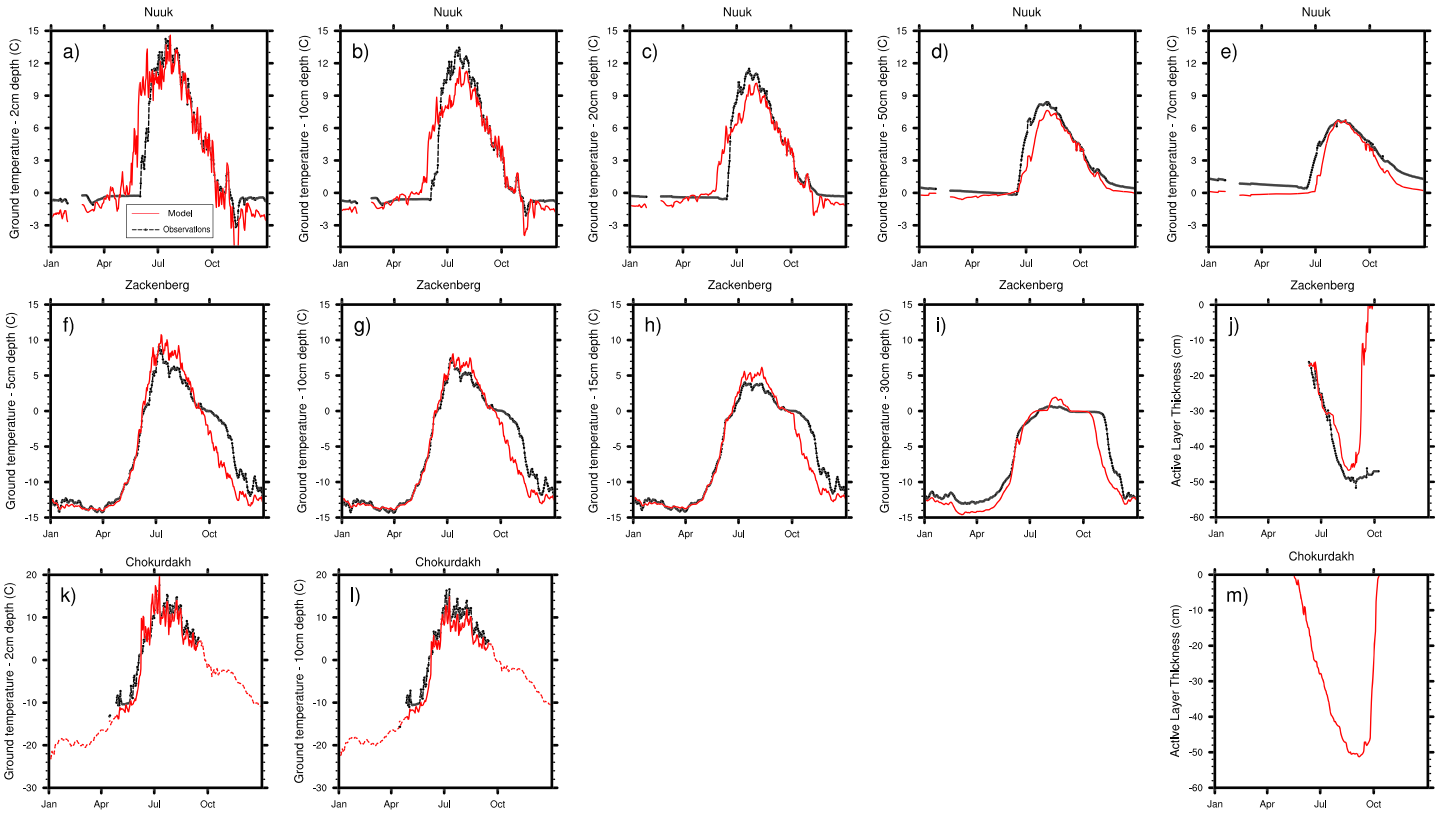

Figure 5. Mean annual cycles of daily ground temperature at several depth on Nuuk (a–e), Zackenberg (f–j), and Chokurdakh (k–m). On Chokurdakh (k) and (l), dotted lines represent the model results for the full experiment period regardless of missing data. Active layer depth is shown for Zackenberg (j) and Chokurdakh (m). At Chokurdakh, active layer depth data are missing.

the model was also reduced from 0.3 in the standard version to 0.1. The amplitude of the seasonal cycle of LAI is greatly improved, with peak values around 1.3 at Nuuk and 0.9 at Zackenberg, but the approximately 1 month delay in leaf onset, peak, and senescence is not improved.

4.2. Radiative Fluxes, Turbulent Fluxes, and Snow Depth

At Nuuk, the flux tower where radiative and turbulent fluxes are measured is located at the border of the fen. At Zackenberg, it is not in the fen but it gives a general sense of the energy balance at the site. Figure 4 shows mean annual cycles of daily latent heat, sensible heat, net radiation, and snow depth for the three studied sites. Corresponding skill scores are shown in Table 4.

The net radiation fluxes are well reproduced at Nuuk and Zackenberg ($r = 0.95$ and 0.93, respectively (Table 4)). At Chokurdakh, the model performs slightly worse ($r = 0.87$), due to September, when modeled net radiation decreases too early (Figure 4i).

At Nuuk, the model tends to have an early snowmelt with respect to observations (Figure 4j). This induces an early increase in soil temperature (Figures 5a and 5b) and an early increase in the sensible heat flux (Figure 4d). This early increase of the sensible heat flux is also present at Chokurdakh (Figure 4f), but the absence of snow depth data does not allow it to be attributed to snowmelt date.

The latent heat fluxes are fairly well simulated at Nuuk and Chokurdakh ($r = 0.64$ and 0.65, respectively). At Zackenberg, the model starts too late and there is a 1-month delay between the modeled and the observed seasonal peaks (Figure 4b, $r = 0.55$) due to the delayed seasonal cycle of LAI (Figure 3b).

4.3. Temperature and Active Layer Thickness

Apart from the early increase due to the early snowmelt at Nuuk, the evolution of temperatures is overall well simulated at every depth for the two greenlandic sites (Figure 5), with correlations over 0.9 (Table 5). At Zackenberg, the model represents the beginning of the zero-curtain period in the fall (Mastepanov et al., 2013) but is unable to reproduce its entirety (Figures 5h and 5i). This might be due to the missing insulation

Table 5
Daily Skill Scores for Temperature at Different Depths for the Three Study Sites

	Nuuk					Zackenberg				Chokurdakh	
Depth	2 cm	10 cm	20 cm	50 cm	70 cm	5 cm	10 cm	15 cm	30 cm	2 cm	10 cm
n	639	639	639	732	732	1542	1510	2657	1543	837	756
Mean	2.99	2.62	2.52	2.45	2.63	−4.5	−5.8	−5.9	−6.24	5.23	5.39
r	0.90	0.93	0.93	0.97	0.97	0.93	0.93	0.94	0.93	0.96	0.96
c-rmse	2.45	1.81	1.51	0.74	0.57	3.33	2.91	2.71	2.35	2.64	2.75
Bias	−0.1	−0.16	−0.28	−0.61	0.89	−1.13	−0.73	−0.74	−0.94	−1.99	−2.48

Note. The number of days with nonmissing data (*n*), observed mean, correlation (*r*), centered root-mean-square error (c-rmse), and bias are shown.

effect of mosses and lichens (Druel et al., 2017) or to processes specific to arctic snow not taken into account in the model. Barrere et al. (2017) show that the ISBA snow scheme has a too strong snow densification, leading to higher thermal conductivity of the basal layer, faster soil freezing, and ultimately a too short zero-curtain period.

The active layer thickness (ALT) is of crucial importance because it is where the main biogenic processes occur. In Zackenberg, the model reproduces the observed ALT fairly well, except in the late season when it freezes too early, as already mentioned (Figure 5j). We do not have active layer data in Chokurdakh, but the literature reports depths around 40–50 cm in wet locations (Budishchev et al., 2014; Parmentier et al., 2011; van der Molen et al., 2007) while the model simulates ALTs around 50 cm.

4.4. Mean Annual CO_2 and CH_4 Fluxes

The CO_2 fluxes simulated by the multilayer and the old bulk carbon models are very similar during the growing season, when photosynthesis is a much larger flux than soil respiration (Figures 6a, 6d, and 6g). At Nuuk, the simulated peak value tends to be more negative than the observed one, indicating a too strong photosynthesis. The models (old and new) also overestimate the flux in the end of summer at both Greenland sites, linked to the LAI (Figure 3). At Nuuk, differences appear right after the snowmelt, when the discretized model produces higher CO_2 fluxes than the bulk model, due to a higher heterotrophic respiration, slightly degrading model performances. The opposite happens at the end of the growing season when the new discretized model performs slightly better. The new model degrades correlation ($r = 0.82$ versus $r = 0.75$; Table 4) but slightly improves the centered rmse and the bias (c-rmse = 145.2 and bias = −39.2 versus 130 and −36.5 respectively). At Zackenberg, there are late-season bursts of CO_2 (Mastepanov et al., 2008, 2013), discussed later. At this site, going from bulk to discretized model degrades CO_2 fluxes after August but improves them before (Figure 6d). Similar to Nuuk, the discretized model performs slightly worse ($r = 0.64$ versus 0.62 when late-season bursts are taken into account in the calculations, $r = 0.92$ versus 0.86 otherwise). At Chokurdakh, data are missing and the discretized model produces higher fluxes.

At all three sites, most of the methane exchanges occur during the period between June and September (JJAS) (Figures 6b, 6e, and 6h). These 4 months account for 75% of the annual methane flux at Nuuk and 98.2% and 92.9 % at Zackenberg and Chokurdakh, respectively. At Nuuk and Zackenberg, the amplitude of CH_4 fluxes is well reproduced (Figures 6b and 6e). At Nuuk, the annual peak is modeled with a 1 month delay (see section 5).

At Zackenberg, there are significant variations of methane fluxes between chambers within a 15-m radius, due to different moisture conditions and microtopographic specificities (Pirk et al., 2017; Skov, 2014). The model cannot reproduce the late-season bursts observed in some years, such as 2007 or 2009 (Figure 7b). It has been hypothesized that frost is the main driver of these emissions: a double-freezing front, upward from permafrost table and downward from the surface, creates high-pressure between them (Mastepanov et al., 2008, 2013). As total gas pressure in soil is not calculated by the model (see section5), it cannot reproduce these late-season emissions, which can contribute significantly to the annual methane budget (Zona et al., 2016) and are thus an important challenge for future modeling work. Nevertheless, the amplitude of modeled methane fluxes is overall satisfying, and when these bursts are removed from skill calculations, it significantly improves the results ($r = 0.74$ versus $r = 0.18$).

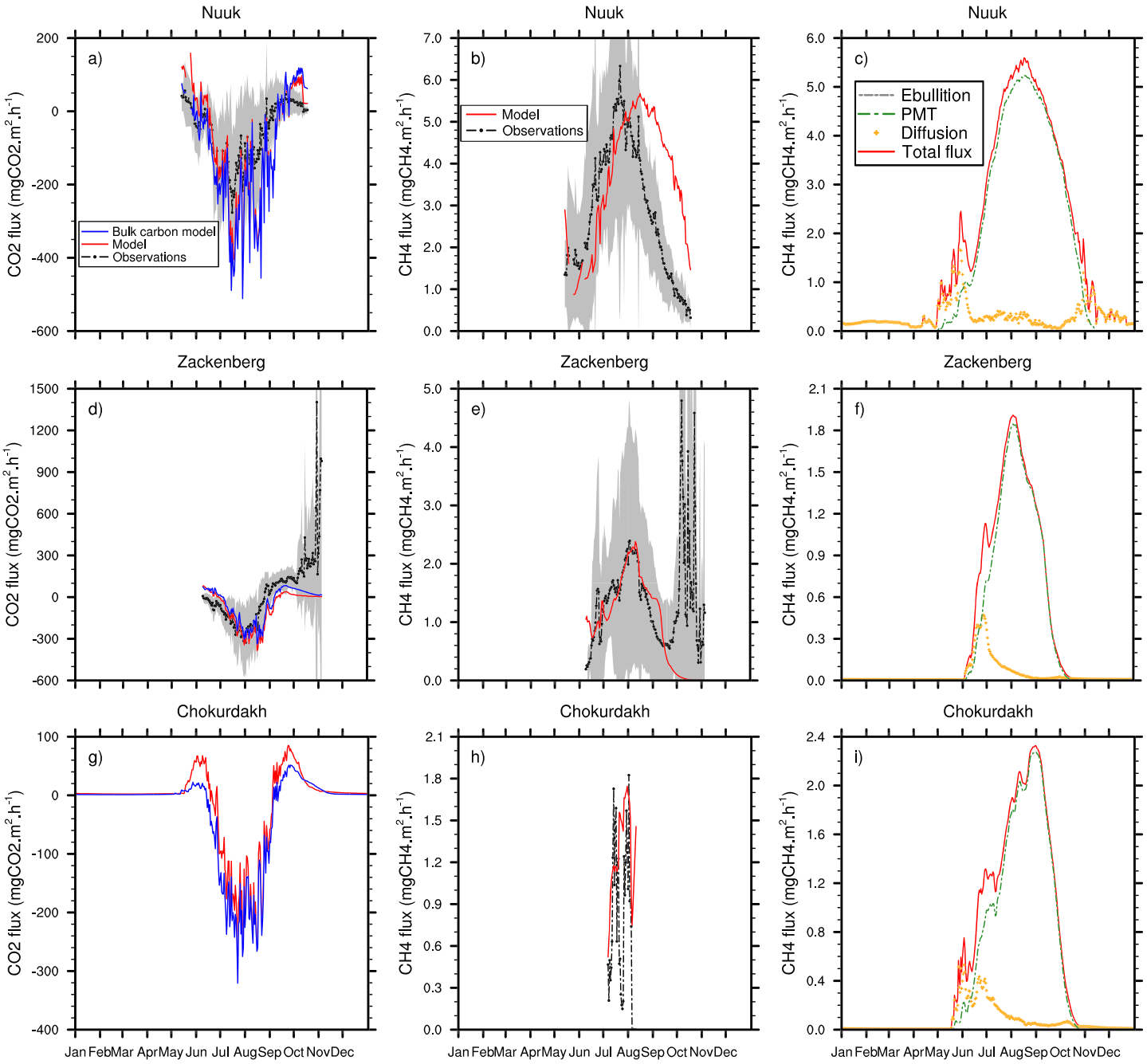

Figure 6. Mean annual cycles of daily carbon dioxide fluxes (a, d, g), daily total methane fluxes (b, e, h), and the relative contribution of diffusion, ebullition, and plant-mediated transport (c, f, i) on Nuuk (top row), Zackenberg (middle row), and Chokurdakh (bottom row). The gray zone represents the 95% confidence interval for the observations when more than one automatic chamber is active (see Appendix C). At Chokurdakh (g), CO_2 observed data are missing. Panels (c), (f), and (i) represent mean annual cycle for the full period of experiment. PMT = plant-mediated transport.

At Chokurdakh, data are much more sporadic due to the use of manual closed chambers (Budishchev et al., 2014; Parmentier et al., 2011). The mean annual cycle is not informative, and the full time series is presented in section 4.5.

At the three sites, methane transport behavior remains essentially the same (Figures 6c, 6f, and 6i). PMT is the main pathway from soil to atmosphere, taking up to 80% of the total flux. This is coherent with the range found by Bhullar et al. (2013) and Knoblauch et al. (2015), while Kutzbach et al. (2004) report a contribution of up to 66%. In accordance with the findings of Riley et al. (2011), we found that the transpiration flux r_{transp}

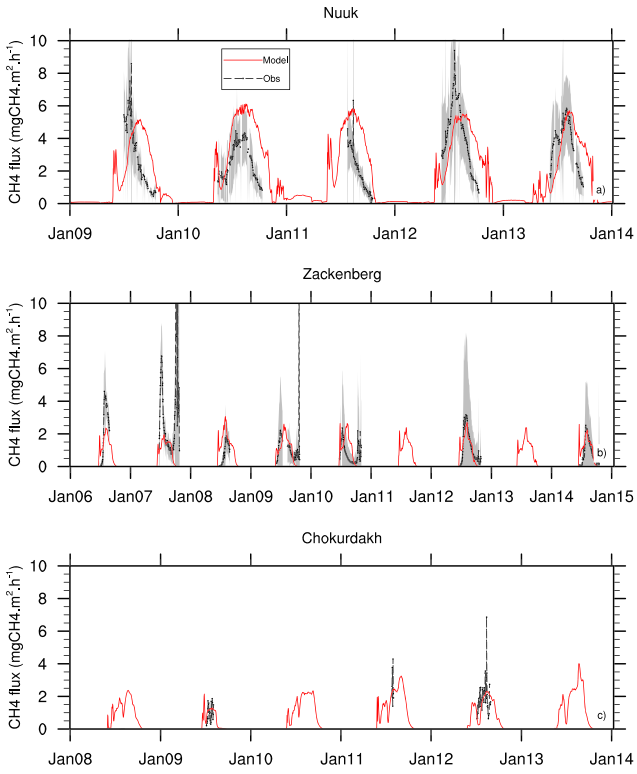

Figure 7. (a–c) Daily methane fluxes over the full observations period for each site. The gray zone represents the 95% confidence interval for the observations when more than one automatic chamber is active (see Appendix C).

accounts for a negligible fraction of the total methane flux, much less than 1%. For the purpose of clarity, its contribution is added to the PMT flux in the rest of the paper, including the figures. Diffusion is the second transport mechanism and is at its highest right after snowmelt, when PMT is not yet efficient. Ebullition does not contribute directly to the exchanges at the soil-atmosphere interface, but we will later show on that it contributes to methane transport within the soil.

4.5. Interannual Variability of CH_4 Fluxes

At Nuuk, the model interannual variability is smaller than the observed one, with annual peak values ranging from 5 to 6 $mgCH_4$/hr versus 4.5 to 9.5 $mgCH_4$/hr (Figure 7a). The winter fluxes in 2010–2011 and 2012–2013 are discussed in section 5.

At Zackenberg, while observed methane fluxes exhibit a strong interannual variability that is not easily explained by the usual environmental variables (Mastepanov et al., 2013), the model interannual variability is also smaller. Whereas some years are particurarly well reproduced (e.g., 2009, 2012, and 2015), the model does not replicate some specificities, such as the high methane flux observed in 2007 or the late-season bursts. At Chokurdakh, the sporadic methane data do not allow us to draw conclusions as to the model's ability to reproduce the interannual variability, but the modeled amplitude is consistent with the range of the observations (Figure 7c).

To summarize, the discretized carbon model slightly degrades CO_2 fluxes compared to the old bulk carbon. CH_4 fluxes are well reproduced overall, and the magnitude of the different transport pathways for CH_4 is coherent with current knowledge.

5. Discussions

Methane fluxes are reproduced well by the model, but we have to check if the processes underlying these fluxes are coherent with current knowledge. In other words, does the model obtain the right fluxes with the right mechanisms? To document the behavior of the model, we present the daily evolution of soil profiles for gases, environmental variables, and biogeochemical processes at Nuuk for the full observation period

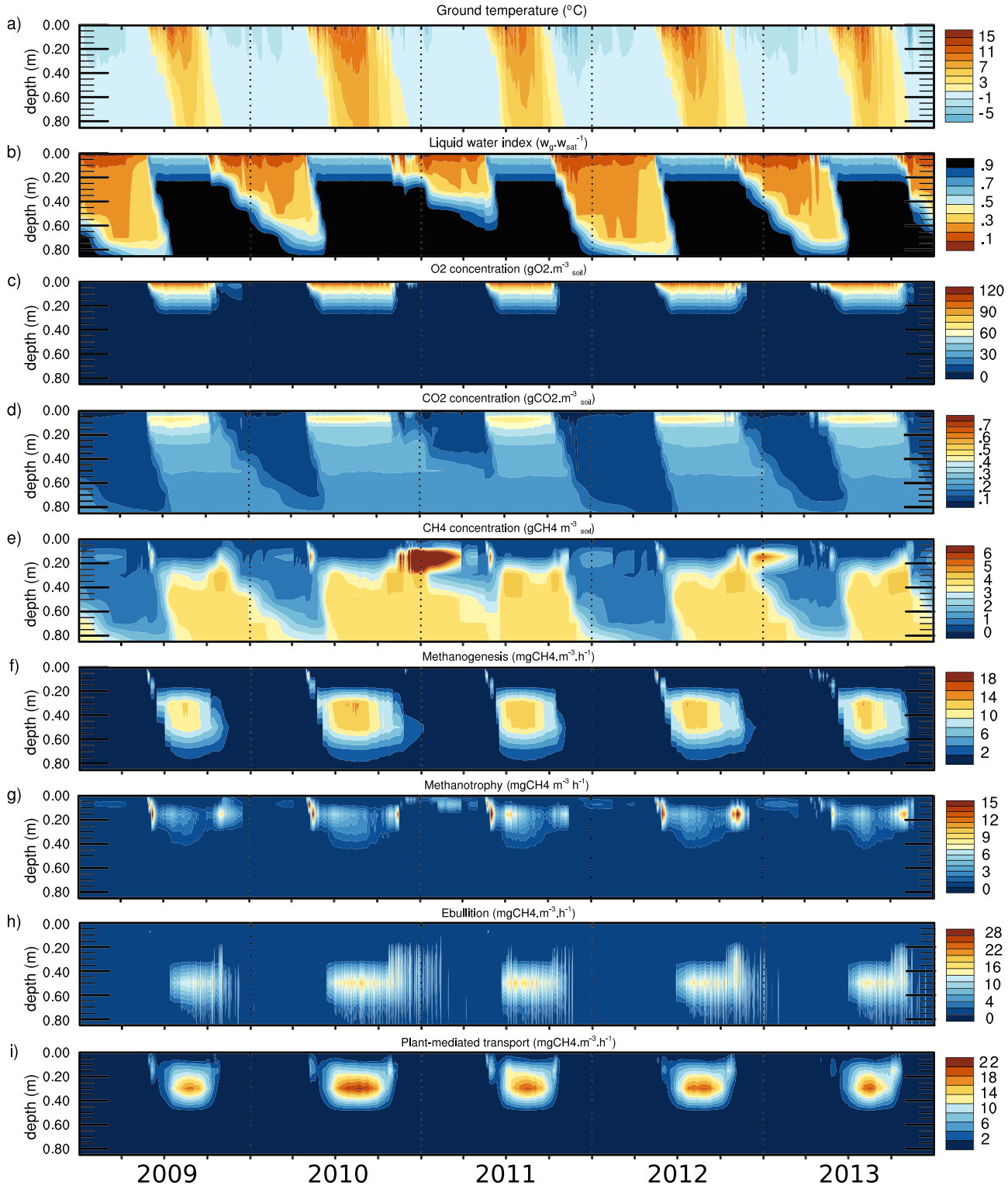

Figure 8. Time versus depth diagram at the Nuuk site over the period 2009–2014 of daily (a) ground temperature, (b) liquid water index w_g/w_{sat}, (c–e) Total gas concentrations per unit soil volume including both the aqueous and gaseous phases (i.e., $\varepsilon_{O_2} O_2$, $\varepsilon_{CO_2} CO_2$, and $\varepsilon_{CH_4} CH_4$), (f) methanogenesis, (g) methanotrophy, (h) methane flux removed by ebullition, and (i) by plant-mediated transport. Dotted vertical lines represent the first day of each calendar year. Each calendar year is divided into four subperiods of 3 months each.

(2009–2014) and at Zackenberg for a shorter period (2006–2011) for the purpose of clarity (Figures 8 and 9, respectively).

As expected, the main biogenic activities (methanogenesis and methanotrophy) occur in the warmer season for both sites, that is, around July–August. Gas profiles of O_2 and CH_4 are coherent with what is observed in the field (Askaer et al., 2011; Preuss et al., 2013): water content and O_2 concentrations are tightly coupled, because diffusion strongly decreases when moisture level rises. O_2 penetration depth is one of the main drivers for methanogenesis and methanotrophy, along with oxic decomposition. Methanogenesis occurs below the water table in the anaerobic zone. Higher methanotrophy occurs near the aerobic/anaerobic interface, because substrate from the anaerobic (methane) and aerobic zone (dioxygen) are both needed for this process (Segers, 1998). PMT bypasses the oxic zone where methanotrophy happens by transporting methane directly from the saturated zone to the atmosphere. At Nuuk, 15% of the methane production is oxidized by methanotrophs, compared to only 7% at Zackenberg. This is probably due to the smaller temperature range at Zackenberg, which inhibits the methanotrophs more. The highest CO_2 bulk concentration is found in the oxic zone, where it is produced by oxic decomposition. CO_2 can, however, diffuse below its production zone, to the anoxic saturated zone, due to its relatively high solubility which increases potential storage in the soil (Tang et al., 2010). At Zackenberg, where permafrost is present, all these processes occur solely inside the active layer, above approximately 40–50 cm (Figure 9).

At Nuuk, the seasonal cycle of the methane flux is too wide, particularly in autumn, and delayed by 1 month (Figure 7). This weakness is not explained by the soil temperatures, which are correctly simulated (Figure 5), nor by the snowmelt date, which tends to be earlier than the observations (Figure 4j). This is partly due to the 1-month delay of modeled LAI at Nuuk, which influences PMT strength, and to the forced water table at 20 cm, which may overestimate water content in the soil during the autumn season, artificially boosting methanogenesis and therefore fluxes. The late decrease is not present in Zackenberg: temperatures are much lower and the freezing process, which is well represented, limits methanogenesis.

At Nuuk, high soil methane concentration occurs during some winters at 20-cm depth, in particular from December 2010 to January 2011 and slightly less in winter 2012–2013 (Figure 8). In these years, December soil temperature is higher and methanogenesis remains active near a depth of 60 cm. Produced methane is transported upward by ebullition up to 20 cm. Finally, because of the combined effects of a slow diffusion due to high ice content and the nonexistent PMT at this period (see equation (29) and Figure 3), the remaining methane takes several weeks to be diffused to the atmosphere, explaining the small methane fluxes during the winters of 2010–2011 and 2012–2013 (Figure 7).

For gas concentrations, the thin first layer (1 cm) is never fully saturated and is always close to equilibrium with the atmosphere. Hence, the ebullition condition is never reached in the top soil, explaining the noninexistant ebullition flux (Figure 6). At Nuuk, ebullition still occurs in the deepest soil layers during the growing season (Figure 8h). Bubbles formed in these layers travel through the soil matrix until ebullition conditions are not satisfied anymore, increasing the velocity at which methane is transported from the depth to the atmosphere. At Zackenberg, the model does not simulate ebullition at any depth as CH_4 concentration never reaches the ebullition threshold, while Mastepanov et al. (2013) noted some rapid CH_4 concentration change events in the Zackenberg fen, potentially due to ebullition, but not exceeding 1% of the total seasonal flux.

We can therefore question whether our simple ebullition threshold is realistic enough. Indeed, ebullition parametrization can be refined in many ways by, for instance, taking into account peat structure (Chen & Slater, 2015). In our view, the most satisfying ebullition algorithm is implemented in the four-substance gas model of Tang et al. (2010), which computes total gas pressure in the soil (i.e., the sum of partial pressures of O_2, CO_2, CH_4, and N_2) and triggers ebullition when this pressure is higher than the sum of atmospheric and hydrostatic pressure. Thus, ebullition is a common process for all the gases. Our model does not represent N_2 and the nitrogen cycle. By using the total gas soil pressure algorithm of Tang et al. (2010) in our framework, we fix the N_2 concentration in the soil, neglecting the variations of the most prominent gas in the soil. This is why, as a first approach, we chose to use the partial pressure of methane, proportional to methane concentration, as a trigger for methane ebullition instead of a total soil gas pressure we cannot yet compute properly. Consequently, we do not compute ebullition for gases other than CH_4 using their partial pressure to avoid a different ebullition behavior for every gas.

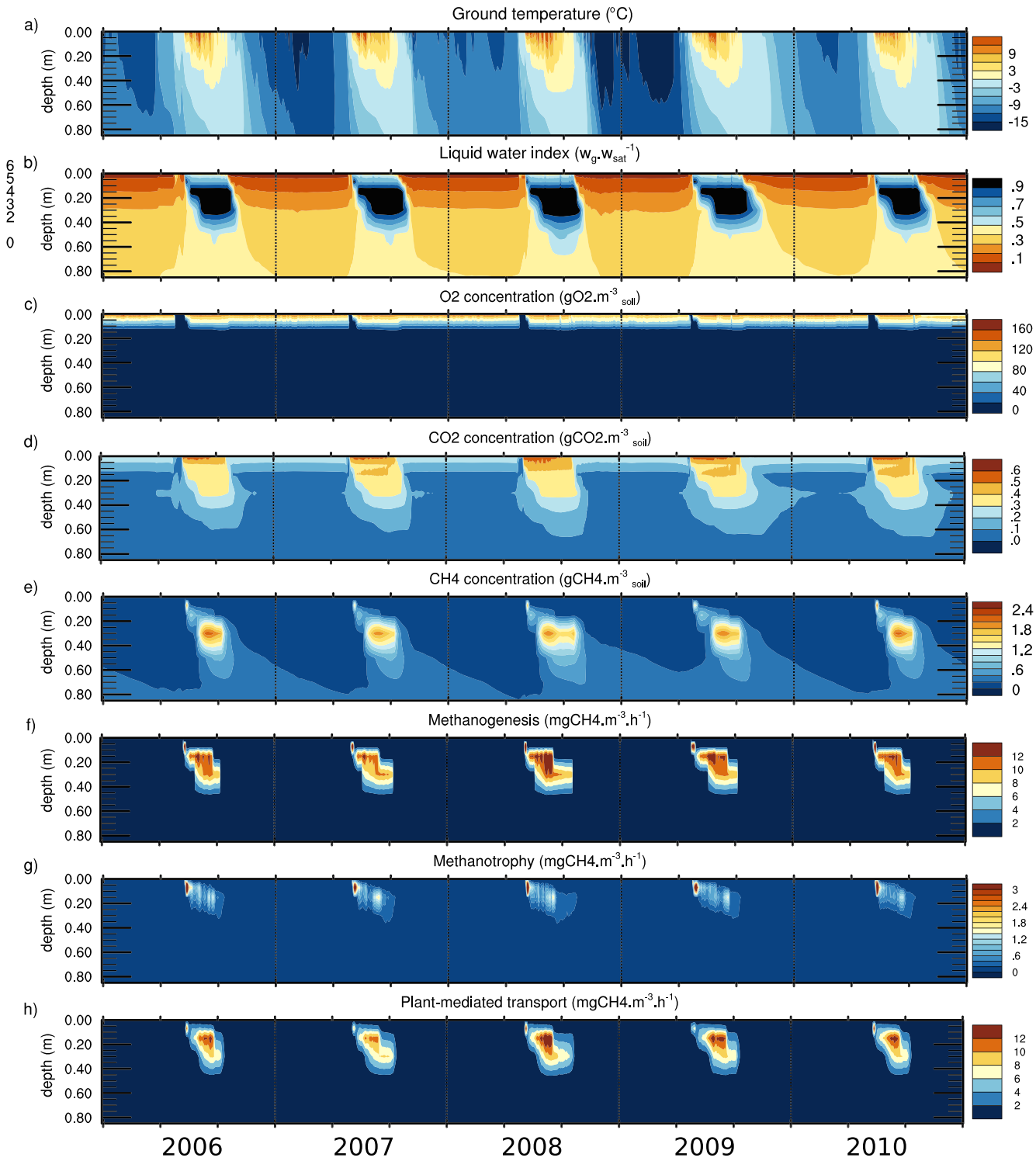

Figure 9. Time versus depth diagram over the period 2006–2011 at the Zackenberg site of daily (a) ground temperature, (b) liquid water index w_g/w_{sat}, (c–e) total gas concentrations per unit soil volume including both the aqueous and gaseous phases (i.e., $\varepsilon_{O_2} O_2$, $\varepsilon_{CO_2} CO_2$ and $\varepsilon_{CH_4} CH_4$), (f) methanogenesis, (g) methanotrophy, and (h) methane flux removed by plant-mediated transport. Dotted vertical lines represents the first day of each calendar year. Each calendar year is divided into four 3-month subperiods.

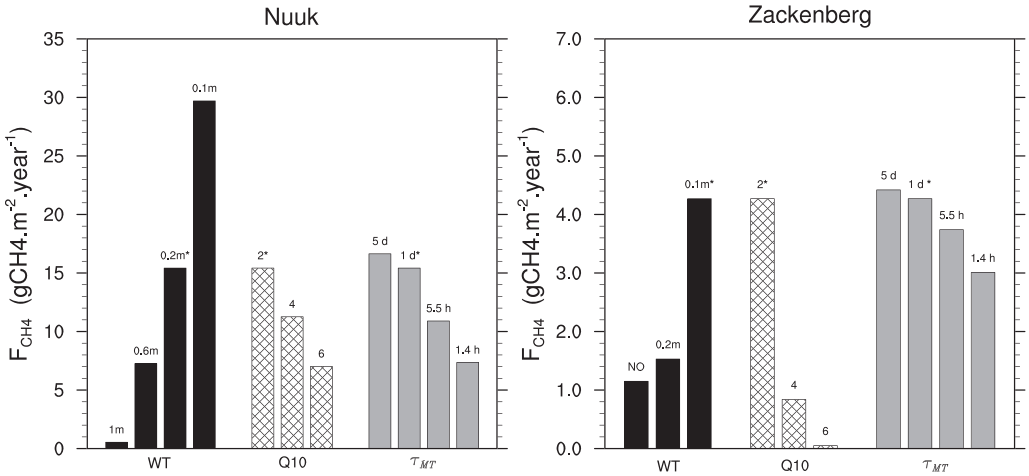

Figure 10. Mean annual values of total methane flux at Nuuk (left) and Zackenberg (right) for different water table depths (WT), Q_{10} value for methanogenesis, and methanotrophy time constant τ_{MT} in days (day) and hours (hr). Asterisks (*) represent the baseline parameters values of reference simulations.

Despite the good model behavior found over field sites, some of the experimental choices such as the imposed water table depth (WTD) remain questionable. Similarly, we can question some parameters related to biogeochemical processes for which the literature reports a large variation range. For each sensitivity experiment described below, we run a 1,500-year spin-up starting from empty carbon pools.

First, we investigate the influence of the WTD at Nuuk and Zackenberg to document the model's response to the hydrology that is likely to change in the future. As explained in section 3.4, at Nuuk and Zackenberg we had to force the saturation below a certain level because the water table is not simply the result of the local water balance. We perform additional simulations with different WTD. At Nuuk, we choose WTD of 1, 0.6, 0.2, and 0.1 m, corresponding, respectively, to a mean degree of soil moisture saturation over 1 m of 0.72, 0.82, 0.94, and 0.97 during the JJAS period which is accountable for 75% of total annual CH_4 fluxes (section 4.4). At Zackenberg, we test how the model reacts without imposing a WTD and with a WTD of 0.2 and 0.1 m, corresponding, respectively, to mean soil moisture saturation values of 0.90, 0.93, and 0.97 over JJAS, when 98.2% of the methane fluxes occurs. At this site, the small differences in soil moisture saturation between no water table and a WTD of 0.2 (0.90 versus 0.93, i.e., a ratio of 1.03) shows that the hydrological properties of permafrost soils are reproduced well. Permafrost acts as an impermeable layer, with an active layer depth of approximately 40–50 cm (Figure 5j) and the frozen conditions below the active layer prevent liquid water from drainage in the deepest layers of the soil, leaving the soil saturated below approximately 20 cm.

For both sites, a deeper water table results in smaller methane fluxes (Figure 10). Indeed, a less saturated soil increases O_2 penetration depth, favoring oxic decomposition, inhibiting methanogenesis and favoring methanotrophy. This effect is particularly pronounced at Nuuk, where a low WTD of 1 m produces 55 fewer methane fluxes compared to a WTD of 0.1 m ($0.54\ gCH_4 \cdot m^{-2} \cdot year^{-1}$ versus $29.7\ gCH_4 \cdot m^{-2} \cdot year^{-1}$), although the ratio between the soil moisture saturations (0.72 and 0.97, respectively) is only 1.35. At Zackenberg, large differences in fluxes also exist between a water level forced at 10 cm and with nothing imposed: methane fluxes are multiplied by 3.7 (4.27 versus 1.15 $gCH_4 \cdot m^{-2} \cdot year^{-1}$), when soil water index varies from 0.90 to 0.97, that is, a 1.18 ratio. Hence, the model is very sensitive to the hydrology.

Second, we investigate the influence of the temperature dependency function of methanogenesis. As noted by Portner et al. (2010) in a bulk carbon framework, the choice of the temperature dependency function for oxic decomposition influences the modeled carbon stocks and CO_2 fluxes. Methane fluxes are too likely to be sensitive. Instead of testing different temperature functions such as the Arrhenius or the Lloyd-Taylor equations (Portner et al., 2010), we chose to keep the exponential Q_{10} formulation and vary the Q_{10} from 2, 4, and 6 (Figure 2a) which is the range reported in Segers (1998) for methane production in minerotrophic peats. We perform additional experiments with these Q_{10} values. The temperature dependency for oxic decomposition remains unchanged.

At both sites, higher Q_{10} values decrease methane fluxes (Figure 10), due to a lower methanogenesis (see equation (23)) and Figure 2a). More precisely, at Nuuk, the mean intensity of the methanogenesis temperature dependency function in JJAS over the first 40 cm is 0.211, 0.047, and 0.020 for Q_{10} values of 2, 4, and 6, respectively, that is, a tenfold reduction. Methane fluxes at Nuuk are divided by 2.2 (15.42 versus 7.02 $gCH_4 \cdot m^{-2} \cdot year^{-1}$). At Zackenberg, these intensities are, respectively, 0.144, 0.22, and 0.008 (i.e., are divided by 18). Methane fluxes are divided by 85 when the Q_{10} varies from 2 to 6, and for the latter experiment, methane fluxes are almost nonexistent (4.72 versus 0.05 $gCH_4 \cdot m^{-2} \cdot year^{-1}$). This drastic sensitivity at Zackenberg is due to the lower soil temperature (Figure 5) and to the strong nonlinearity of the temperature dependency function of methanogenesis (Figure 2a). In terms of absolute mass loss, going from a Q_{10} value of 2 to 6 lowers modeled methane fluxes at Nuuk by 8.4 $gCH_4 \cdot m^{-2} \cdot year^{-1}$ and by 4.68 $gCH_4 \cdot m^{-2} \cdot year^{-1}$ at Zackenberg.

Lastly, we investigate the influence of the methanotrophy rate τ_{MT} by performing additional experiments with different values found in the literature (see Table 2). At both sites, stronger methanotrophy logically results in fewer methane fluxes (Figure 10). At Nuuk, when τ_{MT} goes from 1.4 hr to 5 days, that is, multiplied by 75, methane fluxes are multiplied by 2.3 (7.36 versus 16.64 $gCH_4 \cdot m^{-2} \cdot year^{-1}$). At Zackenberg, for the same τ_{MT} variation, fluxes are only multiplied by 1.5 (4.42 versus 3.01 $gCH_4 \cdot m^{-2} \cdot year^{-1}$). This indicates a much lower sensitivity to the methanotrophy rate than to the soil moisture or temperature. The relatively small effect of the methanotrophy rate is due to the previously discussed bypassing effect of PMT. The lower sensitivity at Zackenberg is explained by the physics: first, the WTD is higher, resulting in a smaller oxic zone where methanotrophy occurs. Second, methanotrophy is more inhibited at Zackenberg due to lower soil temperatures (Figure 5) and a Q_{10} value of 4.2 (Figure 2).

Finally, besides these uncertainties in environmental and physical processes, biotic factors can also impact the production, oxidation, and transport of methane. These biotic factors are not considered explicitly in this study, as the model does not represent microbial population and biomass. Representing their growth and decay as well as their location in the soil could significantly change the model behavior. The priming effect is an intermediate step for an explicit representation of biotic populations (Guenet et al., 2010). Some models take into account microbial functional groups (Xu et al., 2015) or have a biologically based approach (Grant, 1998) that model the several steps of decomposition processes. Due to the nonrepresentation of biotic factors, some biogenic processes are not represented in current methane modules embedded in land surface models. For instance, we only model one methanogenic process, but it is known that several exist, both anaerobic and aerobic (Le Mer et al., 2001; Serrano-Silva et al., 2014). Similarly, methanotrophic bacteria are quite diverse: up to 56 different species have been identified (Serrano-Silva et al., 2014), and the variability of potential methane oxidation rates may be an intrinsic property of these different methanotrophic bacteria (Segers, 1998). It has also been shown by Cui et al. (2015) that anaerobic oxidation of methane can play a nonnegligible role in the soil methane budget. CO_2 can also be produced in anaerobic hozizons (Treat et al., 2014, 2015; Walz et al., 2017), mainly as a coproduct of organic matter degradation. In that case, dioxygen comes from the degradation of hydrocarbons not represented in the model. The anaerobic CO_2 production rate is usually 2–3 times lower than the aerobic production rate (Bridgham & Richardson, 1992; Moore & Dalva, 1993) and at the current stage we do not reproduce it. We could probably approach it by not imposing a null value for oxic decomposition in equation (8) when dioxygen is missing. While it would certainly be an interesting improvement of the model, it would add degrees of freedom to a model whose primary focus is CH_4.

6. Conclusions

In this work, we present a new biogeochemical module that represents three gases within the soil, interactions, and exchanges between them as well as biogeochemical processes and transport mechanisms leading to CH_4 and CO_2 fluxes. The old bulk carbon module of the land surface model ISBA was vertically discretized and features two vertical dynamics processes, advection, and cryoturbation. The carbon and biogeochemical processes model is further fully coupled with the energy and hydrology module of ISBA. This model presents some interesting features and innovations: unlike many existing multilayer models, the separation between methane production and oxydation zones is not directly based on the water table level. Instead, methanogenesis and methanotrophy use the O_2 concentration calculated by the model. As a result, the WTD does not appear in the model equations. We propose a new temperature-dependent formulation for the methanotrophy using recent field and incubation experiments. We also introduce a new layer-by-layer algorithm

for ebullition instead of an instantaneous transport from the soil to the atmosphere. A new formulation for gas bulk diffusivity is also proposed, closer to experimental results than actual state-of-the art formulations. This new scheme, implemented here in ISBA, is applicable to any LSM with a discretized representation of energy and water budgets within the soil.

Our one-dimensional model is applied offline to three arctic sites with different soil temperature regimes, with and without permafrost. The physical module of ISBA correctly represents thawing and freezing processes and hydrological properties of permafrost soils, such as impeded drainage and wet conditions. Furthermore, without site-specific tuning of parameters related to biogeochemical processes, the model is able to reproduce CH_4 and CO_2 fluxes fairly well. The biogeochemical model consistently represents the main processes taking place through the soil column leading to methane fluxes, and its behavior is logical, explainable, and in agreement with what is observed in the field. However, one has to keep in mind that even if the methane emissions are reproduced reasonably well by the model, the relative importance of sources, sinks, and transport processes leading to this result is quite difficult to apprehend. Indeed, the intrinsic uncertainties of parameters related to living organisms involved in methane production and oxidation are large. Moreover, many feedbacks between them can occur. Hence, a particular effort remains to validate these individual CH_4 processes and their combined effects over depth as they vary substantially in time, space, and with ecosystem types.

Additional experiments described in section 5 show that the model is most sensitive to the soil moisture. The choice of the Q_{10} value for methanogenesis temperature dependency is also important, in particular over cold regions where the growing season soil temperatures are low. This underlines the importance of physical processes and the necessity of robust and realistic physical models. The model is less sensitive to the methanotrophy rate τ_{MT}, which has a highly uncertain range, and the differences in sensitivity found between Nuuk and Zackenberg are mainly explained by the physics. Despite uncertainties and some unrepresented biotic factors, our model can provide an interesting tool and framework from more in-depth future work in a climate change context and for regional/global scale experiments.

Appendix A: List of Main Equation Symbols

Table A1 lists all the equation symbols encountered in the paper, with parameters value when relevant.

Table A1
List of Equation Symbols

Symbols	Descriptions	Units	Value[a]
Δt	Model time step	s	
Δz_j	Thickness of jth soil layer	m	
$C_{a,s,p}$	Active, slow, and passive carbon pool	gC/m^3	
$C_{[ab,bg]\times[s,m]}$	Litter pools (above-ground and below-ground, structural and metabolic)	gC/m^3	
S_i	Input from the vegetation and roots exudates into pool i	gC/m^3	
r_i	Fraction of the decomposed material of the carbon pool i lost as respiration		
f_{ji}	Fraction of carbon pool j transformed into pool i		
F^i_{oxic}	Decomposed carbon in pool	gC/m^3	
τ_i	Characteristic time of oxic decomposition of carbon pool i	s	
k_i	Temperature-dependent rate of oxic decomposition of carbon pool i	s^{-1}	
T_g	Ground temperature	°C	
w_g	Volumetric liquid water content	m^3/m^3	
w_{gi}	Volumetric ice content	m^3/m^3	
w_{wilt}	Wilting point	m^3/m^3	
w_{fc}	Field capacity	m^3/m^3	
w_{sat}	Soil porosity	m^3/m^3	
θ	Dimensionless soil moisture control on oxic decomposition		
θ_{fc}	Dimensionless relative water content to the field capacity		

Table A1 *Continued*

Symbols	Descriptions	Units	Value[a]
θ_{sat}	Dimensionless relative water content to the saturation		
A	Advection velocity	m/s	2 mm/year
D	Cryoturbation diffusion coefficient	m^2/s	
C_{max}	Soil carbon mass corresponding to that of available dioxygen	gC/m^3	
X	Dummy gas variable to represent either CH_4, CO_2, or O_2		
$[X]$	Concentration of X in gaseous phase	gX/m^3_{air}	
H^{cc}_X	dimensionless Henry's solubility constant of X		
H^{cp}_X	Henry's solubility	$mol{\cdot}m^{-3} \cdot Pa^{-1}$	
B_X	Bunsen coefficient of X		
R	Universal gas constant	$J{\cdot}mol^{-1} \cdot K^{-1}$	8.314
ϵ_X	Total porosity of X	m^3/m^3_{soil}	
D^a_X	Diffusivity of X in air	m^2/s	
D^w_X	Diffusivity of X in water	m^2/s	
D_X	Diffusivity of X in the bulk medium	m^2/s	
η_a	Permeability in nonsaturated porous media		
η_w	Permeability in saturated porous media		
b	Clapp-Hornberger shape parameter		
M_X	Molar mass of X	gX/mol	
p_s	Atmospheric surface pressure	Pa	
T_s	Atmospheric surface temperature	K	
CH_{4s}	Methane mixing ratio		1.7 ppm
O_{2s}	Dioxygen mixing ratio		20.9%
g_{snow}	Snow-dependence function		
f_{snow}	Grid cell fraction covered by the snow		
ρ_{snow}	Density of the lowest snow layer		
ρ_{ice}	Density of ice		
r_{oxic}	Carbon dioxide produced by oxic decomposition	$gCO_2 \cdot m^{-3}_{soil} \cdot s^{-1}$	
r^X_{transp}	Concentration change due to transpiration	$gX{\cdot}m^{-3}_{soil} \cdot s^{-1}$	
F_{transp}	Water transported by transpiration	$kg{\cdot}m^{-3} \cdot s^{-1}$	
ρ_w	Water volumic mass	kg/m^3	
$r_{MG,i}$	Methane production from carbon pool i by methanogenesis	$gCH_4 \cdot m^{-3}_{soil} \cdot s^{-1}$	
$f(T_g)$	Temperature dependency function for methanogenesis		
T_{lim}	Threshold for $f(T_g)$ linear decrease	°C	1
$g\left(O_2\right)$	Dioxygen dependency function for methanogenesis		
$O_{2,lim}$	Dioxygen threshold for methanogenesis	gO_2/m^3_{water}	2
r_{MT}	Methane oxidation by methanotrophy	$gCH_4 \cdot m^{-3}_{soil} \cdot s^{-1}$	
τ_{MT}	Methanotrophy characteristic time	s	1 day
k_{MT}	Methanotrophy temperature-dependent rate	s^{-1}	
K_{O_2}	Michaelis-Menten constant for dioxygen	mol/m^3	2
K_{CH_4}	Michaelis-Menten constant for methane	mol/m^3	
V_{max}	Potential methane oxidation rate	$mol{\cdot}m^{-3} \cdot s^{-1}$	
X_{ebu}	Ebullition threshold	$gCH_4 \cdot m^{-3}_{air} \cdot s^{-1}$	
r_{CH_4}	Saturated mixing ratio of CH_4		15%
P_s	Soil pressure		
$\left[CH_4\right]^{ebu}$	potential methane concentration subject to ebullition	$gCH_4 \cdot m^{-3}_{air} \cdot s^{-1}$	
V_e	Bubble velocity	m/s	

Table A1 *Continued*

Symbols	Descriptions	Units	Value[a]
r^X_{PMT}	Concentration change due to PMT	$\mathrm{gX{\cdot}m^{-3}_{soil}\cdot s^{-1}}$	
$f^{X,i}_{\mathrm{PMT}}$	Flux of X transported by roots and plants for a layer i	$\mathrm{gX{\cdot}m^{-3}_{soil}\cdot s^{-1}}$	
Π_a	Aerenchyma permeability		1
$\alpha_{\mathrm{CH_4}}$	Nonusability coefficient of CH_4 by the plant		1
$\alpha_{\mathrm{CO_2}}$	Nonusability coefficient of CO_2 by the plant		1
$\alpha_{\mathrm{O_2}}$	Nonusability coefficient of O_2 by the plant		0.3
ρ_r	Aerenchyma porosity		0.3
f^{root}_j	Root fraction in layer j		
f_{veg}	Soil vegetated fraction		
h(LAI)	Leaf area index (LAI) dependency function for PMT		
r_a	Aerodynamic resistance	s/m	0
r_L	Ratio of root length to depth		3

[a]If model parameter.

Appendix B: Bulk Diffusivities

The different bulk diffusivites plotted in Figure 2c followed these equations:

$$D_{X,\mathrm{arithmetic}} = \frac{\nu D^a_X \eta_a + w_g D^w_X H^{cc}_X \eta_w}{\nu + w_g} \tag{B1a}$$

$$D_{X,\mathrm{threshold}} = \begin{cases} \frac{\nu^{\frac{10}{3}}}{w^2_{\mathrm{sat}}} D^a_X, & \text{if } w_g \le 0.95 w_{\mathrm{sat}} \\ D^w_X, & w_g > 0.95 w_{\mathrm{sat}} \end{cases} \tag{B1b}$$

$$D_{X,\mathrm{Nielson}} = \left[\frac{(\nu + w_g)\sqrt{D^a_X D^w_X}}{\nu \sqrt{D^w_X} + w_g \sqrt{D^a_X}} \right]^2 \tag{B1c}$$

Note that since Wania et al. (2010) and Nielson et al. (1984) do not use the dual-phase formulation and the equilibrium hypothesis between the aqueous and gaseous phases, Henry's constants are not present in equations (B1b) and (B1c). Although rewriting their equivalent in the dual-phase framework is straightforward, for the figure, we preferred the original unaltered equations and fixed H^{cc}_X at 1 in equations (B1a) and (12), as our goal is mainly to illustrate the shape of the curves.

Note also that the threshold diffusivity (equation (B1b)) used in Wania et al. (2010) do not use the Moldrup et al. (2003) approach to take into account the soil structure and porosity but instead uses Millington and Quirk (1961). The model CLM4Me (Riley et al., 2011) uses both of these methods depending on the soil type.

Appendix C: Calculation of the 95% Confidence Interval

In this paper, hourly CH_4 fluxes are the mean over all automatic chambers. The number of functioning chambers varies in time. When more than one automatic chamber is active at a time step, the standard deviation between active automatic chambers of the measurement is also provided.

For a fixed day, we consider the hourly standard deviation to be constant, as hourly standard deviation values do not fluctuate much. Taking the number of active automatic chambers into consideration, hourly standard deviations are pooled together to give unbiased estimates of the daily mean standard deviation θ_d. Finally, under the gaussian hypothesis, the 95% confidence interval is defined as $I = \bar{x}_d \pm 1.96 \times \theta_d$ where $\bar{x}_d$ is the observed daily mean.

Acknowledgments
This work was supported by the Acceleration of Permafrost Thaw (APT) project through BNP Paribas Foundation, grant 2014-00000004300. This work was also supported by the H2020 project CRESCENDO "Coordinated Research in Earth Systems and Climate: Experiments, kNowledge, Dissemination and Outreach", which received funding from the European Union's Horizon 2020 research and innovation program under grant agreement 641816. Finally, the Institut Français du Danemark (AFD) supported this work though the grant 15/2017/CSU.8.2.1. We are grateful to Juri Palmtag for providing detailed soil texture and organic layer depth data on Zackenberg and for his valuable insights on Zackenberg soil characteristics. We also thank Guy Schurgers and Roland Seferian for valuable input on earlier versions of the model. Finally, we thank Florent Dominé for his always relevant comments and critiques on the manuscript. Fluxes, radiative, and physical data from Nuuk and Zackenberg sites are freely available on the Greenland Ecosystem Monitoring database website http://data.g-e-m.dk/. Chokurdakh data are public and open access at http://www.europe-fluxdata.eu/. LAI data are from MODIS Land Product subset tool ORNL DAAC. 2017. MODIS Collection 6 Fixed Sites Subsetting and Visualization Tool. ORNL DAAC, Oak Ridge, Tennessee, USA https://doi.org/10.3334/ORNLDAAC/1567. The model is an open source. The SURFEX version 8 used in this work is available to download via the SURFEX platform http://www.umr-cnrm.fr/surfex/. The authors declare that they have no conflicts of interest.

References

Angel, R., Claus, P., & Conrad, R. (2011). Methanogenic archaea are globally ubiquitous in aerated soils and become active under wet anoxic conditions. *The International Society for Microbial Ecology Journal*, *14*(1-2), 59–72. https://doi.org/10.1038/ismej.2011.141

Arah, J. R., & Stephen, K. D. (1998). A model of the processes leading to methane emission from peatland. *Atmospheric Environment*, *32*(19), 3257–3264. https://doi.org/10.1016/S1352-2310(98)00052-1

Askaer, L., Elberling, B., Jrgensen, C. J., Joensen, H. P., Küuhl, M., Glud, R. N., & Lauritsen, F. R. (2011). Linking soil O_2, CO_2, and CH_4 concentrations in a wetland soil: Implications for CO_2 and CH_4 fluxes. *Environmental Science & Technology*, *45*(8), 3393–3399. https://doi.org/10.1021/es103540k

Barrere, M., Domine, F., Decharme, B., Morin, S., Vionnet, V., & Lafaysse, M. (2017). Evaluating the performance of coupled snow-soil models in SURFEX v8 to simulate the permafrost thermal regime at a high arctic site. *Geoscientific Model Development*, *10*(9), 3461–3479. https://doi.org/10.5194/gmd-10-3461-2017

Bhullar, G. S., Edwards, P. J., & Olde Venterink, H. (2013). Variation in the plant-mediated methane transport and its importance for methane emission from intact wetland peat mesocosms. *Journal of Plant Ecology*, *6*(4), 298–304. https://doi.org/10.1093/jpe/rts045

Bohn, T. J., Melton, J. R., Ito, A., Kleinen, T., Spahni, R., Stocker, B. D., et al. (2015). WETCHIMP-WSL: Intercomparison of wetland methane emissions models over west Siberia. *Biogeosciences*, *12*(11), 3321–3349. https://doi.org/10.5194/bg-12-3321-2015

Boone, A., & Etchevers, P. (2001). An intercomparison of three snow schemes of varying complexity coupled to the same land surface model: Local-scale evaluation at an alpine site. *Journal of Hydrometeorology*, *2*(4), 374–394. https://doi.org/10.1175/1525-7541(2001)002<0374:AIOTSS>2.0.CO;2

Boone, A., Masson, V., Meyers, T., & Noilhan, J. (2000). The influence of the inclusion of soil freezing on simulations by a soil vegetation atmosphere transfer scheme. *Journal of Applied Meteorology*, *39*(9), 1544–1569. https://doi.org/10.1175/1520-0450(2000)039<1544:TIOTIO>2.0.CO;2

Bridgham, S. D., & Richardson, C. J. (1992). Mechanisms controlling soil respiration (CO_2 and CH_4) in southern peatlands. *Soil Biology and Biochemistry*, *24*(11), 1089–1099. https://doi.org/10.1016/0038-0717(92)90058-6

Broecker, W. S., & Peng, T.-H. (1974). Gas exchange rates between air and sea. *Tellus*, *26*(1-2), 21–35. https://doi.org/10.3402/tellusa.v26i1-2.9733

Budishchev, A., Mi, Y., van Huissteden, J., Belelli-Marchesini, L., Schaepman-Strub, G., Parmentier, F. J. W., et al. (2014). Evaluation of a plot-scale methane emission model using eddy covariance observations and footprint modelling. *Biogeosciences*, *11*(17). https://doi.org/10.5194/bg-11-4651-2014

Burke, E. J., Hartley, I. P., & Jones, C. D. (2012). Uncertainties in the global temperature change caused by carbon release from permafrost thawing. *The Cryosphere*, *6*(5), 1063–1076. https://doi.org/10.5194/tc-6-1063-2012

Burke, E. J., Jones, C. D., & Koven, C. D. (2013). Estimating the permafrost-carbon climate response in the CMIP5 climate models using a simplified approach. *Journal of Climate*, *26*(14), 4897–4909. https://doi.org/10.1175/JCLI-D-12-00550.1

Calvet, J., Noilhan, J., Roujean, J., Bessemoulin, P., Cabelguenne, M., Olioso, A., & Wigneron, J. (1998). An interactive vegetation SVAT model tested against data from six contrasting sites. *Agricultural and Forest Meteorology*, *92*, 92–95.

Cao, M., Marshall, S., & Gregson, K. (1996). Global carbon exchange and methane emissions from natural wetlands: Application of a process-based model. *Journal of Geophysical Research*, *101*(D9), 14,399–14,414. https://doi.org/10.1029/96JD00219

Chanton, J. P., Bauer, J. E., Glaser, P. A., Siegel, D. I., Kelley, C. A., Tyler, S. C., et al. (1995). Radiocarbon evidence for the substrates supporting methane formation within northern Minnesota peatlands. *Geochimica et Cosmochimica Acta*, *59*(17), 3663–3668. https://doi.org/10.1016/0016-7037(95)00240-Z

Chen, X., & Slater, L. (2015). Gas bubble transport and emissions for shallow peat from a northern peatland: The role of pressure changes and peat structure. *Water Resources Research*, *51*, 151–168. https://doi.org/10.1002/2014WR016268

Ciais, P., Sabine, C., Bala, G., Bopp, L., Brovkin, V., Canadell, J., et al. (2013). Carbon and other biogeochemical cycles. In T. Stocker et al. (Eds.), *Climate Change 2013: The Physical Science Basis. Contribution of Working Group I to the Fifth Assessment Report of the Intergovernmental Panel on Climate Change* (pp. 465–570). Cambridge, United Kingdom and New York, NY: Cambridge University Press. https://doi.org/10.1017/CBO9781107415324.015

Clapp, R. B., & Hornberger, G. M. (1978). Empirical equations for some soil hydraulic properties. *Water Resources Research*, *14*(4), 601–604. https://doi.org/10.1029/WR014i004p00601

Colmer, T. D. (2003). Long-distance transport of gases in plants: A perspective on internal aeration and radial oxygen loss from roots. *Plant Cell & Environment*, *26*(1), 17–36. https://doi.org/10.1046/j.1365-3040.2003.00846.x

Cui, M., Ma, A., Qi, H., Zhuang, X., & Zhuang, G. (2015). Anaerobic oxidation of methane: An "active" microbial process. https://doi.org/10.1002/mbo3.232

Decharme, B., Boone, A., Delire, C., & Noilhan, J. (2011). Local evaluation of the interaction between soil biosphere atmosphere soil multilayer diffusion scheme using four pedotransfer functions. *Journal of Geophysical Research*, *116*, D20126. https://doi.org/10.1029/2011JD016002

Decharme, B., Brun, E., Boone, A., Delire, C., Le Moigne, P., & Morin, S. (2016). Impacts of snow and organic soils parameterization on northern Eurasian soil temperature profiles simulated by the ISBA land surface model. *The Cryosphere*, *10*(2), 853–877. https://doi.org/10.5194/tc-10-853-2016

Decharme, B., Martin, E., & Faroux, S. (2013). Reconciling soil thermal and hydrological lower boundary conditions in land surface models. *Journal of Geophysical Research: Atmospheres*, *118*, 7819–7834. https://doi.org/10.1002/jgrd.50631

Schneider Von Deimling, T., Grosse, G., Strauss, J., Schirrmeister, L., Morgenstern, A., Schaphoff, S., et al. (2015). Observation-based modelling of permafrost carbon fluxes with accounting for deep carbon deposits and thermokarst activity. *Biogeosciences*, *12*(11), 3469–3488. https://doi.org/10.5194/bg-12-3469-2015

Druel, A., Peylin, P., Krinner, G., Ciais, P., Viovy, N., Peregon, A., et al. (2017). Towards a more detailed representation of high-latitude vegetation in the global land surface model orchidee (orc-hl-vegv1.0). *Geoscientific Model Development*, *10*(12), 4693–4722. https://doi.org/10.5194/gmd-10-4693-2017

Duval, B., & Goodwin, S. (2000). Methane production and release from two New England peatlands. *International microbiology: The official journal of the Spanish Society for Microbiology*, *3*(2), 89–95.

Etminan, M., Myhre, G., Highwood, E. J., & Shine, K. P. (2016). Radiative forcing of carbon dioxide, methane, and nitrous oxide: A significant revision of the methane radiative forcing. *Geophysical Research Letters*, *43*, 12,614–12,623. https://doi.org/10.1002/2016GL071930

FAO, ISRIC, ISSCAS, & JRC (2012). Harmonized world soil database (version 1.2). FAO, Rome, Italy and IIASA, Laxenburg, Austria.

Garrigues, S., Boone, A., Decharme, B., Olioso, A., Albergel, C., Calvet, J.-C., et al. (2018). Impacts of the soil water transfer parameterization on the simulation of evapotranspiration over a 14-year mediterranean crop succession. *Journal of Hydrometeorology*, *19*(1), 3–25. https://doi.org/10.1175/JHM-D-17-0058.1

Gibelin, A. (2007). Cycle du carbone dans un modèle de surface continentale: Modélisation validation et mise en oeuvre à l'échelle globale (Ph.D. thesis), Université de Toulouse III - Paul Sabatier.

Gibelin, A. L., Calvet, J. C., Roujean, J. L., Jarlan, L., & Los, S. O. (2006). Ability of the land surface model ISBA-A-GS to simulate leaf area index at the global scale: Comparison with satellites products. *Journal of Geophysical Research*, *111*, D18102. https://doi.org/10.1029/2005JD006691

Goudriaan, J. (1986). A simple and fast numerical method for the computation of daily totals of crop photosynthesis. *Agricultural and Forest Meteorology*, *38*, 249–254. https://doi.org/10.1016/0168-1923(86)90063-8

Grant, R. (1998). Simulation of methanogenesis in the mathematical model ecosys. *Soil Biology and Biochemistry*, *30*(7), 883–896. https://doi.org/10.1016/S0038-0717(97)00218-6

Grünfeld, S., & Brix, H. (1999). Methanogenesis and methane emissions: Effects of water table, substrate type and presence of Phragmites australis. *Aquatic Botany*, *64*(1), 63–75. https://doi.org/10.1016/S0304-3770(99)00010-8

Guenet, B., Danger, M., Abbadie, L., & Lacroix, G. (2010). Priming effect: Bridging the gap between terrestrial and aquatic ecology. *Ecology*, *91*(10), 2850–2861. https://doi.org/10.1890/09-1968.1

Guenet, B., Eglin, T., Vasilyeva, N., Peylin, P., Ciais, P., & Chenu, C. (2013). The relative importance of decomposition and transport mechanisms in accounting for soil organic carbon profiles. *Biogeosciences*, *10*(4), 2379–2392. https://doi.org/10.5194/bg-10-2379-2013

Hansen, B. U., Sigsgaard, C., Rasmussen, L., Cappelen, J., Hinkler, J., Mernild, S. H., et al. (2008). Present-day climate at Zackenberg. *Advances in Ecological Research*, *40*, 111–149. https://doi.org/10.1016/S0065-2504(07)00006-2

Hugelius, G., Strauss, J., Zubrzycki, S., Harden, J. W., Schuur, E. A., Ping, C. L., et al. (2014). Estimated stocks of circumpolar permafrost carbon with quantified uncertainty ranges and identified data gaps. *Biogeosciences*, *11*(23), 6573–6593. https://doi.org/10.5194/bg-11-6573-2014

Intergovernmental Panel on Climate Change (2013). *Climate Change 2013: The Physical Science Basis. Contribution of Working Group I to the Fifth Assessment Report of the Intergovernmental Panel on Climate Change*. In T. Stocker et al. (Eds.) (1535 pp.). Cambridge United Kingdom and New York USA: Cambridge University Press. https://doi.org/10.1017/CBO9781107415324

Jackson, R. B., Canadell, J., Ehleringer, J. R., Mooney, H. A., Sala, O. E., & Schulze, E. D. (1996). A global analysis of root distributions for terrestrial biomes. *Oecologia*, *108*, 389–411. https://doi.org/10.1007/BF00333714

Joetzjer, E., Delire, C., Douville, H., Ciais, P., Decharme, B., Carrer, D., et al. (2015). Improving the ISBA CC land surface model simulation of water and carbon fluxes and stocks over the Amazon forest. *Geoscientific Model Development*, *8*, 1709–1727. https://doi.org/10.5194/gmd-8-1709-2015

Jørgensen, C. J., Lund Johansen, K. M., Westergaard-Nielsen, A., & Elberling, B. (2015). Net regional methane sink in High Arctic soils of northeast Greenland. *Nature Geoscience*, *8*(1), 20–23. https://doi.org/10.1038/ngeo2305

Kaiser, S., G⊙ckede, M., Castro-Morales, K., Knoblauch, C., Ekici, A., Kleinen, T., et al. (2016). Process-based modelling of the methane balance in periglacial landscapes (JSBACH-methane). *Geoscientific Model Development*, *10*(1), 333–358. https://doi.org/10.5194/gmd-10-333-2017

Kätterer, T., Reichstein, M., Andrén, O., & Lomander, A. (1998). Temperature dependence of organic matter decomposition: A critical review using literature data analyzed with different models. *Biology and Fertility of Soils*, *27*(3), 258–262. https://doi.org/10.1007/s003740050430

Khvorostyanov, D. V., Krinner, G., Ciais, P., Heimann, M., & Zimov, S. A. (2008). Vulnerability of permafrost carbon to global warming. Part I: Model description and role of heat generated by organic matter decomposition. *Tellus Series B: Chemical and Physical Meteorology*, *60*(B2), 250–264. https://doi.org/10.1111/j.1600-0889.2007.00333.x

Kirschke, S., Bousquet, P., Ciais, P., Saunois, M., Canadell, J. G., Dlugokencky, E. J., et al. (2013). Three decades of global methane sources and sinks. *Nature Geoscience*, *6*(10), 813–823. https://doi.org/10.1038/ngeo1955

Knoblauch, C., Spott, O., Evgrafova, S., Kutzbach, L., & Pfeiffer, E. (2015). Regulation of methane production, oxidation, and emission by vascular plants and bryophytes in ponds of the northeast Siberian polygonal tundra. *Journal of Geophysical Research: Biogeosciences*, *120*, 2525–2541. https://doi.org/10.1002/2015JG003053

Koven, C., Friedlingstein, P., Ciais, P., Khvorostyanov, D., Krinner, G., & Tarnocai, C. (2009). On the formation of high-latitude soil carbon stocks: Effects of cryoturbation and insulation by organic matter in a land surface model. *Geophysical Research Letters*, *36*, L21501. https://doi.org/10.1029/2009GL040150

Koven, C. D., Riley, W. J., Subin, Z. M., Tang, J. Y., Torn, M. S., Collins, W. D., et al. (2013). The effect of vertically resolved soil biogeochemistry and alternate soil C and N models on C dynamics of CLM4. *Biogeosciences*, *10*(11), 7109–7131. https://doi.org/10.5194/bg-10-7109-2013

Koven, C. D., Ringeval, B., Friedlingstein, P., Ciais, P., Cadule, P., Khvorostyanov, D., et al. (2011). Permafrost carbon-climate feedbacks accelerate global warming. *Proceedings of the National Academy of Sciences*, *108*(36), 14,769–14,774. https://doi.org/10.1073/pnas.1103910108

Krinner, G., Viovy, N., de Noblet-Ducoudré, N., Ogée, J., Polcher, J., Friedlingstein, P., et al. (2005). A dynamic global vegetation model for studies of the coupled atmosphere-biosphere system. *Global Biogeochemical Cycles*, *19*, GB1015. https://doi.org/10.1029/2003GB002199

Kutzbach, L., Wagner, D., & Pfeiffer, E.-M. (2004). Effect of microrelief and vegetation on methane emission from wet polygonal tundra, Lena Delta, Northern Siberia. *Biogeochemistry*, *69*(3), 341–362. https://doi.org/10.1023/B:BIOG.0000031053.81520.db

Le Mer, J., Roger, P., Provence, D., & Luminy, D. (2001). Production, oxidation and consumption of methane by soils : A review. *Archaea*, *37*, 25–50. https://doi.org/10.1016/S1164-5563(01)01067-6

Lerman, A. (1979). *Geochemical processes. Water and sediment environments*. New York: Wiley. https://doi.org.10.1017/S0016756800030545

MacDougall, A. H., Avis, C. A., & Weaver, A. J. (2012). Significant contribution to climate warming from the permafrost carbon feedback. *Nature Geoscience*, *5*(10), 719–721. https://doi.org/10.1038/ngeo1573

Masson, V., Le Moigne, P., Martin, E., Faroux, S., Alias, A., Alkama, R., et al. (2013). The SURFEXv7.2 land and ocean surface platform for coupled or offline simulation of earth surface variables and fluxes. *Geoscientific Model Development*, *6*(4), 929–960. https://doi.org/10.5194/gmd-6-929-2013

Mastepanov, M., Sigsgaard, C., Dlugokencky, E. J., Houweling, S., Ström, L., Tamstorf, M. P., & Christensen, T. R. (2008). Large tundra methane burst during onset of freezing. *Nature*, *456*(SP). https://doi.org/10.1038/nature07464

Mastepanov, M., Sigsgaard, C., Tagesson, T., Ström, L., Tamstorf, M. P., Lund, M., & Christensen, T. R. (2013). Revisiting factors controlling methane emissions from high-Arctic tundra. *Biogeosciences*, *10*(11), 5139–5158. https://doi.org/10.5194/bg-10-5139-2013

Meltofte, H., & Rasch, M. (2008). The Study Area at Zackenberg. https://doi.org/10.1016/S0065-2504(07)00005-0

Meltofte, H., & Thing, H. (1996). Zackenberg basic: The climate basis and geobasis programmes. 1st Annual Report 1995, Zackenberg Ecological Research Operations, Danish Polar Center. Ministry of Research and Information Technology.

Melton, J. R., Wania, R., Hodson, E. L., Poulter, B., Ringeval, B., Spahni, R., et al. (2013). Present state of global wetland extent and wetland methane modelling: Conclusions from a model inter-comparison project (WETCHIMP). *Biogeosciences*, *10*(2), 753–788. https://doi.org/10.5194/bg-10-753-2013

Meng, L., Hess, P. G., Mahowald, N. M., Yavitt, J. B., Riley, W. J., Subin, Z. M., et al. (2012). Sensitivity of wetland methane emissions to model assumptions: Application and model testing against site observations. *Biogeosciences*, *9*(7), 2793–2819. https://doi.org/10.5194/bg-9-2793-2012

Millington, R. J., & Quirk, J. P. (1961). Permeability of porous solids. *Transaction of the Faraday Society*, *57*(8), 1200–1207. https://doi.org/10.1039/tf9615701200

Moldrup, P., Olesen, T., Komatsu, T., Yoshikawa, S., Schjonning, P., & Rolston, D. (2003). Modeling diffusion and reaction in soils: X. A unifying model for solute and gas diffusivity in unsaturated soil. *Soil Science*, *168*(5), 321–337. https://doi.org/10.1097/01.ss.0000070907.55992.3c

Moore, T. R., & Dalva, M. (1993). The influence of temperature and water table position on carbon dioxide and methane emissions from laboratory columns of peatland soils. *Journal of Soil Science*, *44*(4), 651–664. https://doi.org/10.1111/j.1365-2389.1993.tb02330.x

Mueller, C. W., Rethemeyer, J., Kao-Kniffin, J., Löppmann, S., Hinkel, K. M., & Bockheim, J. G. (2015). Large amounts of labile organic carbon in permafrost soils of Northern Alaska. *Global Change Biology*, *21*(7), 2804–2817. https://doi.org/10.1111/gcb.12876

Murguia-Flores, F., Arndt, S., Ganesan, A. L., Murray-Tortarolo, G. N., & Hornibrook, E. R. C. (2017). Soil methanotrophy model (MEMO v1.0): A process-based model to quantify global uptake of atmospheric methane by soil. *Geoscientific Model Development Discussions*, *2017*, 1–38. https://doi.org/10.5194/gmd-2017-124

Myhre, G., Shindell, D., Bréon, F.-M., Collins, W., Fuglestvedt, J., Huang, J., et al. (2013). Anthropogenic and natural radiative forcing. Climate change 2013: The physical science basis. Contribution of working group I to the fifth assessment report of the intergovernmental panel on climate change: The physical science basis. Contribution of working group I to the fifth assessment report of 1–44 pp. https://doi.org/10.1017/CBO9781107415324.018

Myneni, R., & Park, T. (2015). MCD15A2H MODIS/Terra+Aqua Leaf Area Index/FPAR 8-day L4 Global 500m SIN Grid v006. NASA EOSDIS Land Processes DAAC, https://doi.org/10.5067/MODIS/MCD15A2H.006

Nielsen, C., Michelsen, A., Ambus, P., Deepagoda, T., & Elberling, B. (2017). Linking rhizospheric CH_4 oxidation and net CH_4 emissions in an arctic wetland based on $^{13}CH_4$ labeling of mesocosms. *Plant and Soil*, *412*(1-2), 201–213. https://doi.org/10.1007/s11104-016-3061-4

Nielson, K. K., Rogers, V. C., & Gee, G. W. (1984). Diffusion of radon through soils: A pore distribution model. *Soil Science Society of America Journal*, *412*(48), 482–487. https://doi.org/10.2136/sssaj1984.03615995004800030002x

Noilhan, J., & Planton, S. (1989). A simple parameterization of land surface processes for meteorological models. *Monthly Weather Review*, *117*(3), 536–549. https://doi.org/10.1175/1520-0493(1989)117<0536:ASPOLS>2.0.CO;2

Palmtag, J., Hugelius, G., Lashchinskiy, N., Tamstorf, M. P., Richter, A., Elberling, B., & Kuhry, P. (2015). Storage, landscape distribution, and burial history of soil organic matter in contrasting areas of continuous permafrost. *Arctic Antarctic, and Alpine Research*, *47*(1), 71–88. https://doi.org/10.1657/aaar0014-027

Parmentier, F. J. W., van Huissteden, J., van der Molen, M. K., Schaepman-Strub, G., Karsanaev, S. A., Maximov, T. C., & Dolman, A. J. (2011). Spatial and temporal dynamics in eddy covariance observations of methane fluxes at a tundra site in northeastern Siberia. *Journal of Geophysical Research*, *116*, G03016. https://doi.org/10.1029/2010JG001637

Parton, W. J., Stewart, J. W., & Cole, C. V. (1988). Dynamics of C, N, P and S in grassland soils: A model. *Biogeochemistry*, *5*(1), 109–131. https://doi.org/10.1007/BF02180320

Peters-Lidard, C. D., Blackburn, E., Liang, X., & Wood, E. F. (1998). The effect of soil thermal conductivity parameterization on surface energy fluxes and temperatures. *Journal of the Atmospheric Sciences*, *55*(7), 1209–1224. https://doi.org/10.1175/1520-0469(1998)055<1209:TEOSTC>2.0.CO;2

Petrescu, A. M., Van Beek, L. P., Van Huissteden, J., Prigent, C., Sachs, T., Corradi, C. A., et al. (2010). Modeling regional to global CH_4 emissions of boreal and arctic wetlands. *Global Biogeochemical Cycles*, *24*, GB4009. https://doi.org/10.1029/2009GB003610

Ping, C. L., Jastrow, J. D., Jorgenson, M. T., Michaelson, G. J., & Shur, Y. L. (2015). Permafrost soils and carbon cycling. *SOIL*, *1*(1), 147–171. https://doi.org/10.5194/soil-1-147-2015

Pirk, N., Mastepanov, M., López-Blanco, E., Christensen, L. H., Christiansen, H. H., Hansen, B. U., et al. (2017). Toward a statistical description of methane emissions from arctic wetlands. *Ambio*, *46*, 70–80. https://doi.org/10.1007/s13280-016-0893-3

Pirk, N., Tamstorf, M. P., Lund, M., Mastepanov, M., Pedersen, S. H., Mylius, M. R., et al. (2016). Snowpack fluxes of methane and carbon dioxide from high Arctic tundra. *Journal of Geophysical Research: Biogeosciences*, *121*, 2886–2900. https://doi.org/10.1002/2016JG003486

Portner, H., Bugmann, H., & Wolf, A. (2010). Temperature response functions introduce high uncertainty in modelled carbon stocks in cold temperature regimes. *Biogeosciences*, *7*(11), 3669–3684. https://doi.org/10.5194/bg-7-3669-2010

Preuss, I., Knoblauch, C., Gebert, J., & Pfeiffer, E.-M. (2013). Improved quantification of microbial CH_4 oxidation efficiency in arctic wetland soils using carbon isotope fractionation. *Biogeosciences*, *10*(4), 2539–2552. https://doi.org/10.5194/bg-10-2539-2013

Raivonen, M., Smolander, S., Backman, L., Susiluoto, J., Aalto, T., Markkanen, T., et al. (2017). Himmeli v1.0: Helsinki model of methane build-up and emission for peatlands. *Geoscientific Model Development*, *10*(12), 4665–4691. https://doi.org/10.5194/gmd-10-4665-2017

Raundrup, K., Aastrup, P., Nyman, J., Lauridsen, T. L., Sander Johannsson, L., Henning Krogh, P., et al. (2010). Nuuk basic: The biobasis programme. In L. Jensen & M. Rasch (Eds.), *Nuuk Ecological Research Operations, 3rd Annual Report* (Vol. 2009). Aarhus University: National Environmental Research Institute.

Riley, W. J., Subin, Z. M., Lawrence, D. M., Swenson, S. C., Torn, M. S., Meng, L., et al. (2011). Barriers to predicting changes in global terrestrial methane fluxes: Analyses using CLM4Me, a methane biogeochemistry model integrated in CESM. *Biogeosciences*, *8*(7), 1925–1953. https://doi.org/10.5194/bg-8-1925-2011

Sander, R. (2015). Compilation of Henry's law constants (version 4.0) for water as solvent. *Atmospheric Chemistry and Physics*, *15*(8), 4399–4981. https://doi.org/10.5194/acp-15-4399-2015

Saunois, M., Bousquet, P., Poulter, B., Peregon, A., Ciais, P., Canadell, J. G., et al. (2016). The global methane budget 2000-2012. *Earth System Science Data*, *8*(2), 697–751. https://doi.org/10.5194/essd-8-697-2016

Schaefer, K., Lantuit, H., Romanovsky, V. E., Schuur, E. A. G., & Witt, R. (2014). The impact of the permafrost carbon feedback on global climate. *Environmental Research Letters*, *9*(8), 085003. https://doi.org/10.1088/1748-9326/9/8/085003

Schimel, J. P. (1995). Plant transport and methane production as controls on methane flux from arctic wet meadow tundra. *Biogeochemistry*, *28*(3), 183–200. https://doi.org/10.1007/BF02186458

Schirrmeister, L., Grosse, G., Wetterich, S., Overduin, P. P., Strauss, J., Schuur, E. A., & Hubberten, H. W. (2011). Fossil organic matter characteristics in permafrost deposits of the northeast Siberian Arctic. *Journal of Geophysical Research*, *116*, G00M02. https://doi.org/10.1029/2011JG001647

Schlesinger, W. H., & Bernhardt, E. S. (2013). Wetland Ecosystems. In elsevier (Ed.), *Biogeochemistry* (pp. 233–274), chap. Wetland ec. Oxford, UK: Academic Press. https://doi.org/10.1016/B978-0-12-385874-0.00007-8

Schuur, E. A. G., McGuire, A. D., Schädel, C., Grosse, G., Harden, J. W., Hayes, D. J., et al. (2015). Climate change and the permafrost carbon feedback. *Nature*, *520*(7546), 171–179. https://doi.org/10.1038/nature14338

Séférian, R., Delire, C., Decharme, B., Voldoire, A., Salas, D., Melia, M., et al. (2016). Chevallier development and evaluation of CNRM Earth system model—CNRM-ESM1. *Geoscientific Model Development*, *9*(4), 1423–1453. https://doi.org/10.5194/gmd-9-1423-2016

Segers, R. (1998). Methane production and methane consumption: A review of processes underlying wetland methane fluxes. *Biogeochemistry*,*41*(1), 23–51. https://doi.org/10.1023/A:1005929032764

Serrano-Silva, N., Sarria-Guzmn, Y., Dendooven, L., & Luna-Guido, M. (2014). Methanogenesis and methanotrophy in soil: A review. *Pedosphere*, *24*, 291–307.

Shangguan, W., Dai, Y., Duan, Q., Liu, B., & Yuan, H. (2014). A global soil data set for Earth system modeling. *Journal of Advances in Modeling Earth Systems*, *6*, 249–263. https://doi.org/10.1002/2013MS000293

Skov, K. (2014). Spatiotemporal variability in methane emission from an Arctic fen over a growing season: Dynamics and driving factors, Student thesis INES.

Smith, L. C. (2004). Siberian peatlands a net carbon sink and global methane source since the Early Holocene. *Science*, *303*(5656), 353–356. https://doi.org/10.1126/science.1090553

Song, C., Xu, X., Sun, X., Tian, H., Sun, L., Miao, Y., et al. (2012). Large methane emission upon spring thaw from natural wetlands in the northern permafrost region. *Environmental Research Letters*, *7*(3), 034009. https://doi.org/10.1088/1748-9326/7/3/034009/

Stams, A., & Plugge, C. (2003). chap. The microbiology of methanogenesis. In D. Reay, P. Smith, & A. van Amstel (Eds.), *The microbiology of methane and climate changes* (Vol. 87, pp. 14–27). London, UK: Earthscan London.

Stephen, K., Arah, J., Thomas, K., Benstead, J., & Lloyd, D. (1998). Gas diffusion coefficient profile in peat determined by modelling mass spectrometric data: Implications for gas phase distribution. *Soil Biology and Biochemistry*, *30*(3), 429–431. https://doi.org/10.1016/S0038-0717(97)00118-1

Tamstorf, M., Iversen, K., Hansen, B., Sigsgaard, C., Fruergaard, M., Andreasen, R., et al. (2008). Nuuk basic: The geobasis programme. In L. Jensen & M. Rasch (Eds.), *Nuuk Ecological Research Operations, 1st Annual Report* (Vol. 2007). Aarhus University: National Environmental Research Institute.

Tang, J. Y., & Riley, W. J. (2014). Technical note: Simple formulations and solutions of the dual-phase diffusive transport for biogeochemical modeling. *Biogeosciences*, *11*(14), 3721–3728. https://doi.org/10.5194/bg-11-3721-2014

Tang, J. Y., Riley, W. J., Koven, C. D., & Subin, Z. M. (2013). CLM4-BeTR, a generic biogeochemical transport and reaction module for CLM4: Model development, evaluation, and application. *Geoscientific Model Development*, *6*(1), 127–140. https://doi.org/10.5194/gmd-6-127-2013

Tang, J., Zhuang, Q., Shannon, R. D., & White, J. R. (2010). Quantifying wetland methane emissions with process-based models of different complexities. *Biogeosciences*, *7*(11), 3817–3837. https://doi.org/10.5194/bg-7-3817-2010

Tans, P. P. (1998). Oxygen isotopic equilibrium between carbon dioxide and water in soils. *Tellus Series B: Chemical and Physical Meteorology*, *50*(2), 163–178. https://doi.org/10.1034/j.1600-0889.1998.t01-1-00004.x

Tokida, T., Miyazaki, T., Mizoguchi, M., Nagata, O., Takakai, F., Kagemoto, A., & Hatano, R. (2007). Falling atmospheric pressure as a trigger for methane ebullition from peatland. *Global Biogeochemical Cycles*, *21*, GB2003. https://doi.org/10.1029/2006GB002790

Treat, C. C., Natali, S. M., Ernakovich, J., Iversen, C. M., Lupascu, M., McGuire, A. D., et al. (2015). A pan-arctic synthesis of CH_4 and CO_2 production from anoxic soil incubations. *Global Change Biology*, *21*(7), 2787–2803. https://doi.org/10.1111/gcb.12875

Treat, C. C., Wollheim, W. M., Varner, R. K., Grandy, A. S., Talbot, J., & Frolking, S. (2014). Temperature and peat type control CO_2 and CH_4 production in alaskan permafrost peats. *Global Change Biology*, *20*(8), 2674–2686. https://doi.org/10.1111/gcb.12572

van Wijk, M. T., Williams, M., & Shaver, G. R. (2005). Tight coupling between leaf area index and foliage N content in arctic plant communities. *Oecologia*, *142*(3), 421–427. https://doi.org/10.1007/s00442-004-1733-x

van der Molen, M. K., van Huissteden, J., Parmentier, F. J. W., Petrescu, A. M. R., Dolman, A. J., Maximov, T. C., et al. (2007). The growing season greenhouse gas balance of a continental tundra site in the Indigirka Lowlands, NE Siberia. *Biogeosciences*, *4*(6), 985–1003. https://doi.org/10.5194/bg-4-985-2007

Walter, B. P., & Heimann, M. (2000). A process-based, climate-sensitive model to derive methane emissions from natural wetlands: Application to five wetland sites, sensitivity to model parameters, and climate. *Global Biogeochemical Cycles*, *14*(3), 745–765. https://doi.org/10.1029/1999GB001204

Walter, B. P., Heimann, M., Shannon, R. D., & White, J. R. (1996). A process-based model to derive methane emissions from natural wetlands. *Geophysical Research Letters*, *23*(25), 3731–3734. https://doi.org/10.1029/96GL03577

Walz, J., Knoblauch, C., Böhme, L., & Pfeiffer, E.-M. (2017). Regulation of soil organic matter decomposition in permafrost-affected siberian tundra soils—Impact of oxygen availability, freezing and thawing, temperature, and labile organic matter. *Soil Biology and Biochemistry*, *110*, 34–43. https://doi.org/10.1016/j.soilbio.2017.03.001

Wania, R. (2007). Modelling northern peatland land surface processes, vegetation dynamics and methane emissions (PhD thesis), UK.

Wania, R., Ross, I., & Prentice, I. C. (2010). Implementation and evaluation of a new methane model within a dynamic global vegetation model: LPJ-WHyMe v1.3.1. *Geoscientific Model Development*, *3*(2), 565–584. https://doi.org/10.5194/gmd-3-565-2010

Wik, M., Varner, R. K., Anthony, K. W., MacIntyre, S., & Bastviken, D. (2016). Climate-sensitive northern lakes and ponds are critical components of methane release. *Nature Geoscience*, *9*, 99–105. https://doi.org/10.1038/ngeo2578

Xu, X., Elias, D. A., Graham, D. E., Phelps, T. J., Carroll, S. L., Wullschleger, S. D., & Thornton, P. E. (2015). A microbial functional group-based module for simulating methane production and consumption: Application to an incubated permafrost soil. *Journal of Geophysical Research: Biogeosciences*, *120*, 1315–1333. https://doi.org/10.1002/2015JG002935

Xu, X., Yuan, F., Hanson, P. J., Wullschleger, S. D., Thornton, P. E., Riley, W. J., et al. (2016). Reviews and syntheses: Four decades of modeling methane cycling in terrestrial ecosystems. *Biogeosciences*, *13*(12), 3735–3755. https://doi.org/10.5194/bg-13-3735-2016

Yang, W. H., McNicol, G., Teh, Y. A., Estera-Molina, K., Wood, T. E., & Silver, W. L. (2017). Evaluating the classical versus an emerging conceptual model of peatland methane dynamics. *Global Biogeochemical Cycles*, *31*, 1435–1453. https://doi.org/10.1002/2017GB005622

Yuan, Y., Conrad, R., & Lu, Y. (2009). Responses of methanogenic archaeal community to oxygen exposure in rice field soil. *Environmental Microbiology Reports*, *1*(5), 347–354. https://doi.org/10.1111/j.1758-2229.2009.00036.x

Zhang, Y., Sachs, T., Li, C., & Boike, J. (2012). Upscaling methane fluxes from closed chambers to eddy covariance based on a permafrost biogeochemistry integrated model. *Global Change Biology*, *18*(4), 1428–1440. https://doi.org/10.1111/j.1365-2486.2011.02587.x

Zhu, Q., Liu, J., Peng, C., Chen, H., Fang, X., Jiang, H., et al. (2014). Modelling methane emissions from natural wetlands by development and application of the TRIPLEX-GHG model. *Geoscientific Model Development*, *7*(3), 981–999. https://doi.org/10.5194/gmd-7-981-2014

Zhuang, Q., Melillo, J. M., Kicklighter, D. W., Prinn, R. G., McGuire, A. D., Steudler, P. A., et al. (2004). Methane fluxes between terrestrial ecosystems and the atmosphere at northern high latitudes during the past century: A retrospective analysis with a process-based biogeochemistry model. *Global Biogeochemical Cycles*, *18*, GB3010. https://doi.org/10.1029/2004GB002239

Zimov, S. A. (2006). Climate change: Permafrost and the global carbon budget. *Science*, *312*(5780), 1612–1613. https://doi.org/10.1126/science.1128908

Zona, D., Gioli, B., Commane, R., Lindaas, J., Wofsy, S. C., Miller, C. E., et al. (2016). Cold season emissions dominate the Arctic tundra methane budget. *Proceedings of the National Academy of Sciences*, *113*(1), 40–45. https://doi.org/10.1073/pnas.1516017113